Investigation of Air Noise in Micro-Loudspeaker Systems

Masterthesis

Paul Berghold

Supervisor: Univ.Prof. Dipl.-Ing. Dr.techn. Alois Sontacchi (IEM)

In collaboration with Sound Solutions International

Graz, June 2022

Affidavit

I declare that I have authored this thesis independently, that I have not used other than the declared sources/resources, and that I have explicitly indicated all material which has been quoted either literally or by content from the sources used. The text document uploaded to TUGRAZonline/KUGonline is identical to the present master's thesis.

21.06.2022

Date

Signature

Abstract

Micro-loudspeaker systems suffer from the growing requirement for higher sound pressures levels, while their application size should decrease. Therefore, an exceeding membrane excursion is required. The high excursion is related to the introduced air velocity in front of the membrane. Further on, sound transmission to the surface is produced via a tube (sound port). In addition to usual speaker non-linearities, turbulences caused by high velocities occur in these tubes. The high-velocity airflow interacts with the sound port geometry, causing flow separation and vortex shedding in the boundary layer of the port wall and at its openings. Because of this, unwanted air noise occurs during the sound transmission. Standard acoustic parameters like the total harmonic distortion (THD) focus on the produced sound's harmonic part, but air noise is highly non-linear and chaotic. Thus standard parameters fail to provide a clear understanding of whether port noise is present or not. Compared to previous research on port noise, a Volt Kalman filter is used to separate the produced sound into its harmonic and non-harmonic components. In this way, the obtained residual signals can be used for further detailed air noise analysis. Thus, this work defines proper measurement conditions and identifies a fingerprint/indicator for port noise caused in micro-speaker systems. The findings are compared to the research conducted on port noise in bass-reflex systems.

Contents

1. Introduction

1.1. Why port noise?

Micro speakers are mainly used in small-scale devices like smartphones or tablets and therefore underly strict space requirements from the manufacturer. Nevertheless, maintaining the necessity to produce high sound pressure levels. The only way to fulfil those requirements is to build high excursion speakers. The exited membrane moves a vast amount of air particles quickly, resulting in high air velocities at the membrane surface. Such speaker systems are commonly mounted somewhere inside the devices and need proper sound transmission to the device surface via a tube, also called sound port (SP). The additional air in front of the membrane interacts with the speaker system and causes changes in the frequency response. For example, acting as a Helmholtz resonator, or observed in the time domain, causing additional small and broadband noise due to turbulent airflow in ports.

The field of aeroacoustics addresses the problem of turbulent air propagation through ports. They provide the theoretical background to the underlying physical phenomenon for the emergence of turbulences, causing port noise. A first evaluation for the presence of port noise is the Reynolds number. This dimensionless parameter predicts the transition from laminar to turbulent airflow in a pipe. The complex geometries in real applications demand a more sophisticated approach. In the time domain, such problems can be simulated by computational fluid dynamics (CFD). Due to the complexity of the numerical solutions for a full three-dimensional spatial model, the CFD suffer from long computation times, reaching multiple days depending on the CPU and used stimuli. The numerical complexity reveals the need for a proper possibility to acoustically measure port noise and define a fingerprint with characteristic signal parameters to detect its occurrence reliably.

For electro-acoustical transducers, it is standard to use a simplified lumped parameter model (LPM) to predict the system's frequency response. The acoustic, electrical and mechanical elements are assumed as tightly coupled. They can be approximated by transforming the mass, compliance and damping into the respective electrical counterparts inductance, capacitance and resistance. The system then can be described using classical electrical network theory, calculating the frequency response and with it, for example, the resonance frequencies.

The simulations mentioned above (CFD and LPM) assume linearity, but port noise is a velocity-driven, non-linear, time-variant, chaotic phenomenon. Measuring such a phenomenon is not trivial. Therefore, this work discusses the best acoustical measuring setup for port noise and shows how to calculate an indicator for port noise classification.

The first task is to find the best measurement setup for a pressure microphone. The positioning concerning the angle and distance of the microphone in relation to the port orifice is investigated thoroughly. Also, the excitation signal, the robustness against unwanted blowing wind effects, and more precisely, the use of a windshield and its alteration of the frequency response are explored. Additional, the overall repeatability of the measurements is tested. A second pressure microphone inside the front volume of the speaker is used for further investigations of the origin of port noise. The velocity and excursion of the membrane are measured with a laser vibrometer and triangulation laser for a sine tone signal, offering more insights into the evolution of noise during excitation. Details on the used equipment and measurement setup are shown in section 2.

Section three of this work investigates raw measurement data to get a first impression of port noise. A Vold Kalman Filter (VKF) is used to separate the measured signals into harmonic and non-harmonic signal components. The remaining filtered residual (non-harmonic signal component) can be used to calculate port noise indicators. This separation shows that standard parameters like the total harmonic distortion (THD), the total harmonic distortion plus noise (THD+N), or higher-order harmonic distortion (HOHD) fail to identify port noise because they merely treat the deterministic/harmonic signal part of the first few harmonics. Port noise, although still annoying to the human ear, is relatively low compared to the level of the first few harmonics (k1 - k10). The domination of the harmonic distortions prevents the detection of air noise in those standard acoustic parameters.

The geometrical shape of the port, in combination with the maximum velocity, defines if the transmitted airflow is turbulent or laminar. At high velocities, the airflow in the port separates. Flow in the boundary layer of the port walls becomes turbulent, and the viscoelastic effect of air cannot bind rising eddies anymore. The chaotic stream of rising and dissolving eddies in the boundary layer leads to vortex shedding. As a result, the air inside the port is excited with an impulse-like disturbance. *"This impulse excites all frequencies in the port, and most critically, it will excite the eigenfrequency of the air inside the port".* [Bez19] Because of the narrow dimensions in micro-speaker ports, the eigenfrequencies of the ports are located in the upper-frequency range (above 8 kHz) and remain negligible. Audible disturbances are caused by small and broadband noise, boosted by the systems frequency response, especially at the first and second resonance frequencies of the micro-speaker system. This noise is demonstrated in the time signals and frequency representations in section 3.

Section three also deals with post-processing and calculating different single value parameters that indicate port noise. The investigated parameters are sound pressure level (SPL), total harmonic distortion (THD), noise energy in the residual, roughness, sharpness and different loudness metrics, each for the original and residual signal.

Finally, section four uses this parameter set to calculate a multidimensional feature matrix over all measurement points. A principal component analysis (PCA) maps the measurements for four different port geometries with varying amplitudes levels onto a two-dimensional plane. With this dimensionality reduction, each port noise measurement can be interpreted regarding the noise level on the first principal component and the noise quality on the second.

A distinct separation of the ports is possible but not over the total frequency range. Due to the substantial velocity dependency, port noise changes dependent on the frequency of the exciting signal, introducing many noise types. Still, it is possible to rate port performances in combination with the noise to signal loudness ratio (NSLR). A distinct level at which port noise becomes audible or disturbing is missing.

1.2. History and difference to existing literature

The theoretical background of air noise can be split into two domains. The first is rooted in the field of aeroacoustics as shown in [How02], [Kal15], providing the mathematical solutions for CFD simulations. The second is built on the more practical acoustical experiments on bass reflex ports, mainly used in this work. Detailed summaries of this scientific field and the research done by various engineers over the last decades can be found in [BDM19], [RD04] and [SDB02]. For the sake of completeness, those findings will be mentioned here again. Most of the citations are taken one by one (*text italic*), but some are truncated and rearranged to keep a chronological structure, avoiding redundancy.

History

> *"In 1968 Ingard and Ising [II67] studied the nature of compression and distortion in orifices.* They showed *...the effects of compression on the SPL with increasing level, the non-linear behavior of high SPL and the resulting harmonic content from a symmetrical orifice driven at high level. Note that the odd harmonics are much stronger, before appreciable distortion due to turbulence ensues. Both authors point to a need for ports to be large in order that they produce greater SPL before losses and distortion become intolerable, the bottom line being to limit the velocity to below about 10 m/s. Both allude to turbulence being generated as the Reynolds number becomes too high, this being the cause of performance degradation. The degradation takes the form of broadband noise, harmonic distortion, and compression."* [1] Compression measurement in their research compared the SPL level between the inlet and outlet of ports.

---

[1] [SDB02]

In 1995 *"Backman [Bac95] compared the performance of ten ports to a typical straight tube mounted to a baffle. He found that a symmetrical port with a flange and a blend radius at each end was optimum. The study also included ports with corners and bends, both of which were found to reduce performance significantly."* [2]

"Vanderkooy developed the calculations needed to find the tuning frequency for both straight and flared port tubes in [Van97] and [Van98]. *He also experimented with ports of various lengths and profiles and demonstrated the chaotic nature of ports operating outside the linear region."* [2] In his work, he shows *"...detailed measurements of port velocities and pressure waveforms, presents waveform analysis, and outlines a detailed methodology for taking the data."*[1] The waveform distortions at progressively higher levels on a straight and a radiused port are shown. *"Note that the straight port develops a rather asymmetrical waveform with high levels of both odd and even harmonics. The radiused (at both ends) port, however, generates a more symmetrical wave, resembling a square wave with largely odd harmonics only. Vanderkooy reports on compression effects on several ports with a variety of interesting mathematical descriptions. While no one profile stands out as superior, an interesting observation of the data (also shown by Backman) shows that at medium to higher levels, a small amount of gain takes place before compression sets in. This might suggest that boundarylayer separation is beginning, but is very small and provides a more aerodynamic flow of the air in the center of the port, which is still laminar."* [1] This could be seen as a hysteresis effect in ports. *"In other words: Once instability sets in one has to lower the drive level significantly in order to restore stability."* [3] *"Vanderkooy shows detailed measurements and analyses of the exit jet formation at high levels."* [1] *"In order to get a better visualization of the flow near the port he used a hot wire anemometer to measure the velocity of air. It was shown that instabilities start to occur when port velocities approach the 5 to 10 m/s range."* [3]

"Roozen et al. continued the research using both experimental and numerical methods to show the flow phenomena within a port [RVN98].

---

[2] [BDM19]

[3] [RD04]

He postulated that boundary layer turbulence and unsteady separation of the acoustic flow at the port termination are the main causes of undesirable blowing noises. From the numerical simulation of the flow through the port it can be seen that vortices occur at the port termination for straight ports and closer to the centre with more generously flared ports." [3] *"Also, the magnitude of the vortices is less in the slow taper port."* [1] It was shown numerically and empirically ..." *that vortex shedding creates an impulsive excitation of the port Eigenfrequencies resulting in unwanted noise at the* $\lambda/2$ *port resonance.*[2] *He concluded that a gently flared port with small radius is the optimum configuration to avoid unwanted effects."* [3]

"In 2002 Salvatti, Devantier and Button presented an extensive history on the subject and conducted several experiments [SDB02]. They concluded that ports with generous flares performed best at low sound levels, and straight ports performed best at very high levels. They also suggested that ports with moderate flares represented the best compromise and performed well over a wide range of sound pressure levels. Both entrance and exit loses were considered to effect the performance of the port. The importance of port symmetry was also highlighted. While the conclusions were clear, and supported by the empirical data and basic fluid flow theory, it was not clear why ports of moderate flare were near optimum." [3]

"Rapoport and Devantier [RD04] used Computational Fluid Dynamics (CFD) to model the unsteady flow of the air in the port. They modelled, built, and measured six ports of various flare rates ranging from straight with blend radii to over-flared." [2] The flow at the inlet of various ports was modelled. It showed that losses become insignificant when the entrance angle approaches approximately 30 degrees, confirming the theoretical optimum known from White [Whi03]. *"Distortion and compression measurements hinted at an optimal design but blind listening tests contradicted the notion that the port with lowest distortion was preferred by listeners."*[2] It was also the port with the most flare.

"More recently, Backman returned to the subject in 2016 [Bac16]. He built a CFD model of a bass reflex loudspeaker system with a straight port and a 160 mm woofer in a 16-liter enclosure. He concluded that the combination of CFD modelling and acoustic-based boundary conditions

> *is capable of describing the qualitative behavior of a ported loudspeaker system. In 2017, he built on his earlier work analyzing the performance of his model over a wide range of sound pressure levels [Bac17]. He was able to model the well-known phenomena of port compression and resonance shift."* [2]
>
> *"In 2017, Garcia-Alcaide et al. [Gar+17] published a paper investigating vortex shedding as a source of port noise using numerical and experimental techniques. They observed noise in the 1 kHz region for a port tuned at 65 Hz."* [2]
>
> *"...Button et al. [But+18] characterized the acoustic mass and the acoustic resistance of two different loudspeaker ports as a function of drive level"*[2] in 2018. They suggested using lookup tables that correlate the mass and resistance with drive level to accurately model the non-linear behaviour of vented boxes with lumped parameter (LP) simulations.

[BDM19], [RD04] and [SDB02]

Revising the inconsistency between objective and subjective testing in Rapoport and Devantiers' paper, Bezzola in 2019 [BDM19] used linear acoustic FEM simulations to solve the Helmholz equations for the ports used in [RD04], avoiding the numerically expensive CFD simulations. He postulated that the best sounding port has the lowest propensity for flow separation and that flow separation is minimal when the RMS particle velocity contours at port exit have minimal curvature. These new simulations match with optimal performance measurements and listening experiences. He also showed that ports with less flare have concave velocity contours, and ports with more flare have convex velocity contours. To further test his hypothesis, he designed eight additional ports and tested them for compression and spectral content around the port eigenfrequencies. As stipulated in [SDB02], [RD04], Bezolla also showed that there is a voltage level where compression is reversed before degrading. Here compression is calculated between the driver peak voltage and acoustic pressure. They assumed that this reversing effect is caused by the onset of turbulence and the air-bearing effect. It is noteworthy that no proof or explanation for the air-bearing effect in ports was found in the literature by the author.

Pene in 2020 [Yve20] proposes *"a method to predict the resulting non-linear* *acoustic losses for a given loudspeaker, enclosure volume and port geometry. The approach consists of coupling computational fluid dynamics (CFD) simulation in time domain with loudspeaker non-linear motion modelization".*

In 2020, Bezzola wrote another paper [And20] *"investigating the acoustic mass and resistance R_{ap} as function of drive level for various ports. The values of these parameters are hard to measure, and previous research indicates that they are both functions of turbulence levels in the port airflow."* He showed that port acoustic mass remains essentially a constant independent of drive level and that port acoustic resistance is related to drive level the same way as port compression and port noise are. Repetitive multi-tone sequences were used to separate noise and non-linear components from the best linear approximation (BLA) of the response and then the frequency response function (FRF) of the BLA was fitted to a linear LPM model. A thorough explanation of this method can be found in [Bru+17]. A decrease of the acoustic mass is demonstrated at intermediate levels before it increases with higher input levels again, confirming previous observations in compression measurements and the assumption of the air bearing effect. The authors explain this effect as follows:

> *At intermediate levels, the air at the port boundary experiences a high shear rate and starts to form turbulent vortices along the port boundary. However, the energy of these vortices is not high enough to propagate across the entire port and cause flow separation. But these vortices can act as an "air bearing", reducing the shear rate in the air outside the turbulent layer.* [And20]

Additional, a novel method for calculating noise with repetitive multi-tone signals is discussed. The variance of the FRFs between repetitions subsequently is taken as a measure of noise. They concluded that unflared and bent ports show a strong dependence of the acoustic resistance R_{ap} (value changes up to 10 dB) with peak drive level. Straight flared ports show only minor variations (2 dB) of R_{ap} to the driver level. The port acoustic mass is approximately constant over all excitation levels. A shift for the first resonance peak is observed for high amplitude levels because of a shift in the stiffness of the membrane K_{ms}. The fitting shows that *"K_{ms} appears to vary more significantly with drive level than R_{ap} for straight flared ports. Because K_{ms} does not vary with port shape,"* they assumed that its drift with drive level is due to the driver's viscoelastic suspension effects. Perhaps this is also an indicator of the membrane's stress caused by adding a port.

Difference to existing literature

The most considerable difference between the existing investigations on port noise and this present work is that most of the experiments mentioned above only calculate standard parameters like THD, total SPL curves, some bandpass filtering around the port resonances, or the compression, but fail to split the measured pressure signal into its harmonic and non-harmonic parts. In this work, such a separation is completed by a VKF, explained in section 3.1, providing time signals for each k-th harmonic and the remaining residual. A close examination of the residual waveform shows a clear indication of when and if noise due to turbulence occurs.

This separation technique enables to listen to the residual signal. The author's initial subjective listening tests indicated that specific characteristic sound features are audible when noise is present. Identifying different noise modes was tested with the objective psychoacoustic parameters, sharpness, and roughness. A MATLAB toolbox for calculating psychoacoustic parameters by Sontacchi [Son98] was used for this reason. Although noise is measurable, it does not mean that it is annoying for the human ear. Is it possible to estimate the cumbersomeness of port noise with an analytical method? Typically, a listening test is very helpful to get an insight into the cumbersomeness. However, they are extremely time extensive and therefore solely impractical for designing a proper sound port for a micro speaker application.

1.3. Nomenclature for sound ports

In this work, the port inlet is the orifice connected to the front volume of the driving speaker. The outlet represents the one side connecting to the free air domain. Air is streaming in and out of the port bidirectional, meaning that the flow changes direction within an excitation period, e.g., sine tone. If the port diameter, in theory, would converge close to zero, the front cavity would typically act as a pressure chamber with constant pressure. Therefore, the impedance difference between the free air domain and the continuous flow streaming out of the port will be more significant at the outlet, causing more turbulences. Figure 1.1 displays the inlet at the front cavity of the speaker, the port neck and the outlet into the acoustic near field.

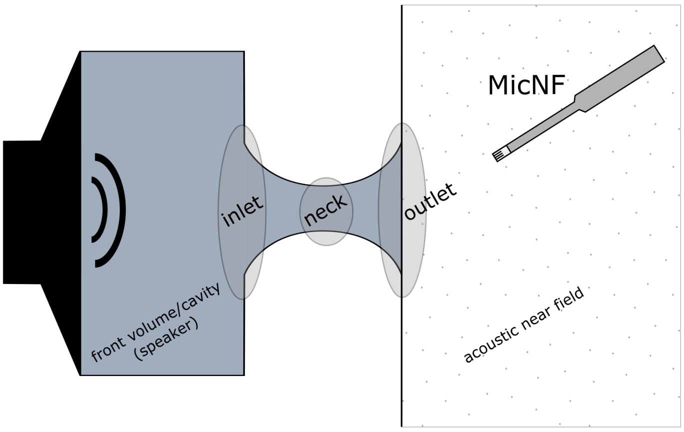

Figure 1.1.: Port measurement setup nomenclature

1.4. Aeroacoustic phenomenons and definitions in sound ports

Transition between laminar and turbulent flow

Noise due to airflow is present if the flow is getting turbulent. Under the assumption of incompressible flow in loudspeaker ports, the primary parameter used to describe the behaviour of all Newtonian fluids, like air, is the Reynolds number *Re*, a dimensionless quantity predicting the transition between laminar and turbulent flow. It is defined as

$$Re = \frac{uL}{\nu} = \frac{\rho u L}{\mu} = \frac{inertial forces}{viscous forces} \tag{1.1}$$

in [SDB02], where ρ is the air density, u is the velocity in [m/s], L is the characteristic length, also referred to as the hydraulic diameter in a pipe, μ is the dynamic viscosity and ν being the kinematic viscosity of the fluid (air). [Whi03, page 294-296]

For the simple example of flow in a straight pipe of diameter $L = r$, experimental observations show that laminar flow occurs when $Re < 2300$ and turbulent flow occurs when $Re > 2900$. [SG16, chapter 15] In between, the flow will transition back and forward, from laminar to turbulent, dependent on the different speeds and conditions of the fluid in the pipe's cross-section. Additionally, the turbulence onset strongly depends on other factors such as pipe roughness and flow uniformity. Laminar flow also tends to dominate the fast-moving centre of the pipe, while slower-moving turbulent flow dominates near the walls. A standard overview of pipe roughness conditions can be found in the so call Moody Diagram [Whi03, page 349]. There is no analytic solution for a more complex geometry's exact onset of turbulent flow. Even numerical simulations struggle with this task, but the above mentioned critical Reynolds numbers are an established approximation for the occurrence of turbulences in loudspeaker ports. Port noise can be assumed to only be present at higher Reynolds numbers.

Turbulences

> "Turbulence can be defined as an eddy-like state of fluid motion where the inertial vortex forces of eddies are larger than other forces, such as viscous or buoyant forces, which arise to damp out the eddies. It leads to random fluctuations in the flow velocity, with amplitude variations of up to 20% of nominal and with a wide frequency band width of "noise" components up to 10 kHz. Physically, turbulence occurs when viscous forces are unable to damp out the non-linear inertial vortex forces"... "that arise in the pipe. Fig. 1.2 illustrates viscous pipe flow. The flow is to the right, and the vortex rings appear clockwise, facing downstream. Note that the direction of the vortex forces is inward, and these are balanced by the viscous forces, which are directed outward. This equilibrium is delicate and can be upset

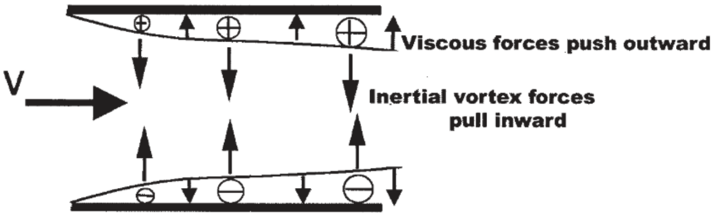

Figure 1.2.: Balance between viscous forces and internal vortex forces [SDB02]

as the velocity increases. Beyond a critical value of *Re* any small perturbation will cause the formation of eddies that are too large to be damped." [SDB02]

Vorticity

The vorticity vector is defined as the curl of the velocity vector. Vorticity is a measure of the rotation of a fluid particle.

Flow separation and vortex shedding

"Several of the studies mentioned in the introduction suggest that flow separation and vortex shedding generate unwanted noise that is most objectionable to listeners. Vortex shedding occurs when the air flow at the exit of the port tube is separating, creating a reversal of flow direction. Flow separation can be described by the stream-wise momentum equation of fluid flows:"

$$u\frac{\delta u}{\delta x} = \frac{dp}{dx} + v\frac{\delta^2 u}{\delta y^2} \tag{1.2}$$

"where u is the velocity along stream lines and x, y, are stream-wise and normal coordinates. Flow reversal is primarily caused by an adverse pressure gradient imposed in the boundary layer. An adverse pressure gradient is $\frac{dp}{dx} > 0$ when shear stress, which

> can be seen to cause the velocity u to decrease along x and possibly go to zero if the adverse pressure gradient is strong enough"... [Bez19]

Figure 1.3 illustrates flow seperation in the boudary layer, with $\delta(x)$ being the boundary layer thickness, $U(x)$ is the velocity profile and τ_w is the wall shear stress.

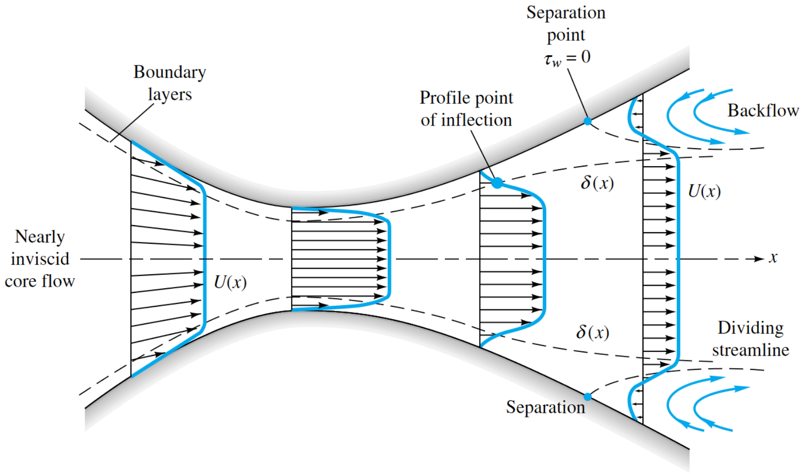

Figure 1.3.: flow seperation in the boundary layer of a port [Whi03]

Summarizing, flow separation or boundary layer separation is the detachment of a boundary layer from a surface. *"The boundary layer separates when it has travelled far enough in an adverse pressure gradient that the speed of the boundary layer relative to the surface has stopped and reversed direction. The flow becomes detached from the surface and instead takes the forms of eddies and vortices."* [Bez19] In sound ports, flow is bi-directional, and therefore the inlet and outlet of the port will change during the oscillating flow patterns. The exact geometry of those openings becomes an interesting design parameter. e.g., *"If a pipe's inlet has a sharp edge flow separation can be expected in a phenomenon known as vena contracta."* [RD04] Moreover, Rapoport explains:

> "Although entrance losses are heavily associated with geometry exit losses are not. Since flow separation is inevitable at the exit, it would be optimum for the flow to separate at the port

> termination. A straight pipe with a sharp edge is the best way to ensure that this will occur. As a result the optimum geometries for entrance and exit are significantly different. Thus, for a bi-directional flow entrance and exit geometry must be considered together in order to find an optimum port profile." [RD04]

Further, the relation between entrance loss for a simple pipe (port) as a function of bend radius and entrance angle can be found in [Whi03, chapter 6.4, page 372]. With the above mention flow phenomenons, the cause for noise due to turbulent flow can be explained like: *"Flow separation leads to vortex shedding, which can excite the air inside the port tubes with an impulse-like disturbance. This impulse excites all frequencies in the port, and most critically, it will excite the eigenfrequency of the air inside the port."* [Bez19].

Port resonator and eigenfrequencies

Adding a port to a speaker acts as a Helmholz Resonator, consisting of the air volume in the front cavity, the port and external air volume. The resonance frequency for this kind of resonator is given by,

$$f_{\text{Helmholtz}} = \frac{c}{2\pi}\sqrt{\frac{S_0}{L_{eff}V}} = \frac{c}{2\pi}\sqrt{\frac{\rho_0}{m_a V}} \tag{1.3}$$

where c is the speed of sound, ρ_0 is the mean density of air, S_0 is the reference cross-sectional area of the port, V is the front volume, L_{eff} is the effective port length defined as

$$L_{eff} = \int_0^L \frac{S_0}{S(x)} dx, \tag{1.4}$$

and m_a is the acoustic mass of the port defined as

$$m_a = \int_0^L \frac{\rho_0}{S(x)} dx. \tag{1.5}$$

In these equations, L is the physical length of the port, x is the axial coordinate along the port axis and $S(x)$ is the cross-sectional area of the port at the axial coordinate x. [RVN98]. In practice, an end correction must be added to consider the moving mass of the external air volume. Generated noise will be particularly enhanced at the Helmholtz frequency $f_{\mathrm{Helmholtz}}$ and the port eigenfrequencies. Examples of typical frequency responses are shown in section 3.3.

Disregarding end corrections the eigenfrequencies of a straight port can be estimated by the half- and quarter-wavelengths,

$$f_{\frac{\lambda}{2}} \approx \frac{c}{2L} \; or \; f_{\frac{\lambda}{4}} \approx \frac{c}{4L}, \tag{1.6}$$

respective. For the investigated port lengths of 10 mm the eigenfrequencies are estimated to be lager than 17.15 kHz or 8.57 kHz respective and are neglectable. Therefore, the exact port eigenfrequencies of a more complex port geometry doesn't need to be considered in simple micro-speaker systems.

2. Measurement setup

Four different sound ports were investigated. They are axisymmetric in the pressure wave propagation direction and were 3D printed at Sound Solutions (SSI) Vienna. The first sound port is a straight tube designed to reference the worst-case scenario. Port three is a funnel-shaped, straight flared port with an increasing diameter from the port inlet to the outlet. This port is closest to real-world applications. Sound ports two and four have an exponentially decreasing and increasing cross-section area, with the latter having a larger diameter. All four port designs are shown in figure 2.1.

Sound Port		SP01	SP02	SP03	SP04
Geometry					
Length:	[mm]	10	10	10	10
Min. diameter:	[mm]	3.2	3.2	3.22	4.35
Min. cross section:	[mm^2]	8	8	8.1	14.9

Figure 2.1.: Investigated sound port designs

Early research of bass reflex ports showed that flared ports perform better than straight ports. It was also demonstrated that radiused edges at the orifice increase performance concerning compression and total SPL before port noise is significant [Bac95], [RVN98] [SDB02]. Here, the investigated port designs are chosen to show distinct differences based on the findings in the literature. The theory conducted from the considerably larger bass reflex ports reasonably approximates what to expect from different port geometries. However, it needs to be proven for micro-speaker ports.

The measurement setup for this work consists of a closed metal casing with a two-inch driver speaker, a fixed back volume and an adapter plate, shown in figure 2.3. Each port can be mounted seamlessly (at the inlet) on this plate. The driver speaker specifications are attached in appendix A. Additionally, a plexiglass cleavage is built into the adapter plate to enable excursion and velocity measurements of the driver membrane with a laser vibrometer (Polytech PSV-400) and a triangulation laser (Keyence LK-H052). Finally, the whole adapter is mounted on a 76 cm times 72 cm baffle. The 3D printed ports do not build a flat plain with the baffle, but the influence of reflections on the surrounding port edge is neglectable.

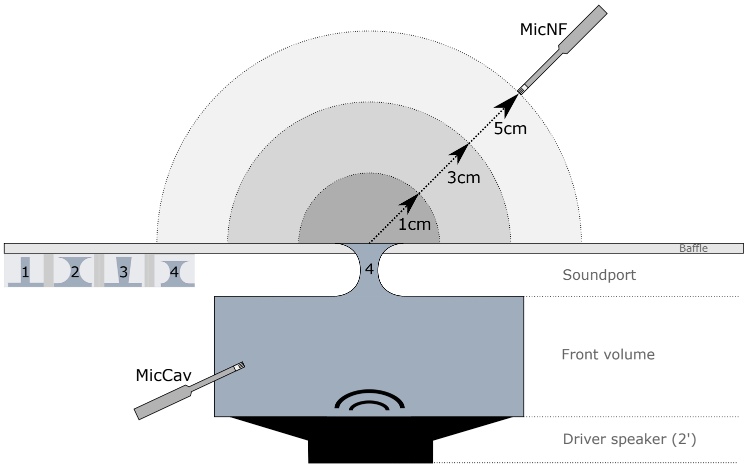

Figure 2.2.: Schematic port noise measurement setup

This specific setup is chosen to minimise the influence of the driver membrane and only measure the differences caused by the ports. Micro speakers, in general, are highly non-linear and would present additional distortions. Therefore, they are not used in this work.

The measurements are performed on the Audio Precision APX 526 multichannel audio analyser using a GRAS 12 AU power amplifier and a Brüel

& Kjær Nexus microphone preamp. Two quarter-inch (63.5 mm) measurement microphones are used to measure the produced noise. One of them is mounted inside the front cavity of the loudspeaker (GRAS Type 26AC), the other in the near field in front of the baffle (Brüel & Kjær Type 2670). Figure 2.3 and 2.2 show the real and schematic measurement setup.

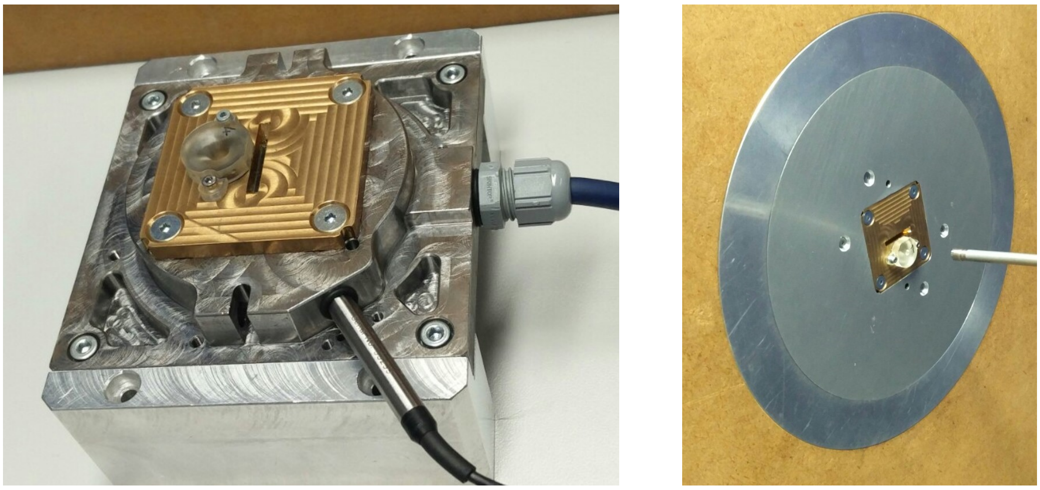

(a) Measurement adapter with cavity mic

(b) Mounted adapter in baffle

Figure 2.3.: Real measurement adapter and mount

The grey hemispheric areas in figure 2.2 indicate three different measurement distances (1, 3, 5 cm) to the port orifice. All measurements are done for three different stimuli. The first being a three-second long continuous sweep with a starting frequency of $f_{start} = 50$ Hz and a stop frequency of $f_{stop} = 20$ kHz. The second is the same parameterized sweep but time-reversed i. e. starting with the highest frequency and stopping with the lowest frequency (from now on called inverse sweep). The third is a 3-second sinusoidal tone with 100 Hz (from now on called 100 Hz sine). The tone at 100 Hz is used because velocity laser measurements at the driver membrane showed that all tested ports have approximately the same input velocity at this frequency. Therefore, it is assumed to be a fair air noise comparison.

2.1. Initial measurements

The driver cone velocity is measured with the Polytech laser to get a first impression of sound port differences. Figure 2.4 shows the continuous sweep excitation at 500 mV peak level. First differences dependent on the port geometry are detected in the electrical impedance of the driver membrane. Probably resulting from a varying acoustic mass between sound ports. The measurement displays two resonance frequencies for each port, corresponding to the driver and port resonance of the combined system. All resonance frequencies, f_{res} are shown in the following table:

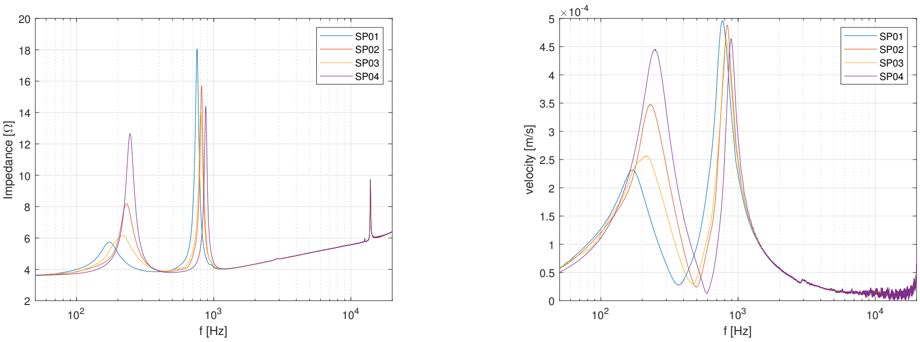

(a) Electrical impedance (b) Velocity

Figure 2.4.: Resonance frequencies of the acoustic system from laser vibrometer measurements with 500 mVp amplitude

Port designs:	SP01	SP02	SP03	SP04
f_{res1} [Hz]:	174	232	216	245
f_{res2} [Hz]:	756	815	805	874

Table 2.1.: Resonance frequencies of the combined system (driver, front volume and port)

Turbulences and following port noise are aeroacoustic phenomena. Considering the wave propagation in the electro acoustic system, it should be possible to gradually investigate the evolution of port noise, starting from excursion to velocity and further from the cavity to near field pressure microphone. The driver cone velocity does not indicate any effects due to turbulences. However, a reaction of the port on the membrane is observed at high input voltages. Further discussion on this effect is completed in section 3.4.

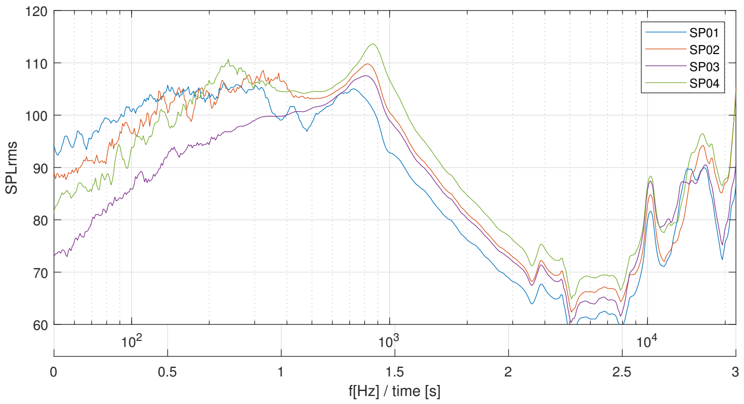

(a) All four sound ports on axis with 1 Vrms sweep excitation

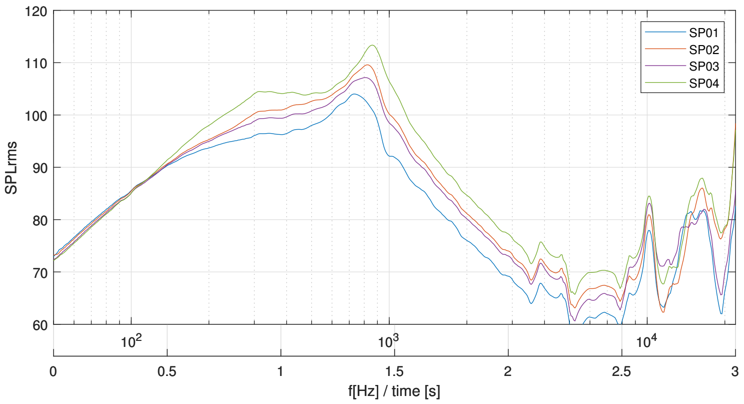

(b) All four sound ports at 60° with 1 Vrms sweep excitation

Figure 2.5.: SPL frequency response

Figure 2.5 and shows the frequency response function (FRF) in dBSPL for all four ports measured with a pressure microphone outside the port. A sweep excitation with 1 Vrms at 0° and 60° is shown in the subfigures 2.5(a) and 2.5(b).

The resonance frequencies measured from the pressure microphone will display minor variations but are close to the laser ones. The calculation method for the FRF is explained in detail in section 3.5. The figures show two axes, the first representing the excitation frequency and the second the corresponding time instant.

Since the length of the sound ports is constant, the primary influence is the diameter and the shape of the opening. The port resonances follow the theory deducted from bass-reflex systems. Ports with smaller diameters and following higher acoustic masses have their resonance peaks at lower frequencies. Similar as shown in equation 1.4 and 1.5 the effective length of a port and its acoustic mass decreases if the port is flared and the blend radius is increased. The port's cross-sectional area $S(x)$ increases, the acoustic mass decreases, and the resonance frequency rises.

The first measurements display the lambda half port resonance $\frac{\lambda}{2}$ at $\approx$ 17 kHz and variations around this frequency due to the different port geometries. The cause for peaks at 4 kHz and 10 kHz is uncertain, but they could originate from reflections in the front volume of the speaker (shown in figure 1.1). The comparison between figure 2.5(a) at 0° and figure 2.5(b) at 60° shows interesting distortions in the lower frequency range under 400 Hz. Also, damping of the frequencies above 4 kHz is visible. The microphone position needs further investigation to ensure an undistorted measurement setup and only measure sound port differences. In appendix B the FRF measurements for all ports and angles are presented. Distinct differences, e.g., in total SPL, low-frequency distortions, and high-frequency damping, can be seen between different geometries. The reasons for these effects are investigated in the following sections.

2.2. Finding the best measurement position

Initial measurements showed that an unwanted air stream occurs at the port orifice with high sound pressure levels. This airstream or blowing noise causes distortions on the microphone membrane. Therefore, it is necessary to find a measurement position that can avoid this effect — maintaining a good

SNR while bearing in mind the general angle dependency of loudspeakers at high frequencies.

The first data set of measurements was taken for the 4 ports under 5 radiation directions ($\alpha = 0°, 15°, 30°, 45°, 60°$) at 3 distances ($r = 1, 3, 5$ cm) with 3 signal levels ($0.1, 1, 2.5$ Vrms) for all 3 excitation signals (sweep, inverse sweep and 100Hz sine). The measurement microphone in the near field of the port is omnidirectional and points directly at the port orifice for all angles. Therefore, all changes due to the microphone angle derive from the directivity pattern of the evaluated ports.

Figure 2.6 shows the measurement setup with the microphone positions and a schematic graphical interpretation of possible measurement distortions with $f(Hz)$ denoting the dependency on the relative angle α between the measurement system and the microphone. This test setup showed that the distance of $r = 1$ cm is too small to prevent distortions with angle variations of the microphone. The distance of $r = 5$ cm decreases the SNR compared to the closer position. For the angle and voltage levels, a more refined grid was necessary.

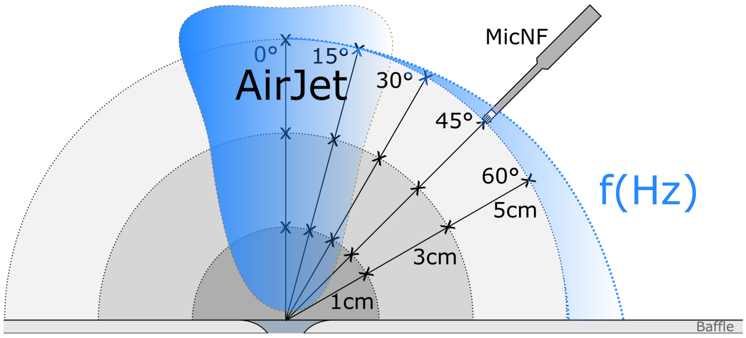

Figure 2.6.: Measurement distortions due to air jet stream and angle dependent damping, indicated by f(Hz)

A second data set of measurements was done with the microphone position fixed to a radius of $r = 3$ cm, reaching a good SNR for all amplitude levels. The amplitude levels are changed to 16 logarithmic voltage steps ranging from 0.2 Vrms to 3.15 Vrms, and the evaluated angular resolution is increased to 5°. All measurement positions were done with and without a windshield, yielding a total of 4992 measurements for the second data set (4 sound ports x 13 angles x 2 windshields = 104 with 16 amplitude levels for each of the three stimuli).

Brixen in 2006 [Bri06] also investigated the noise caused by wind, with air velocities ranging from 5 to 20 m/s. He found that noise due to the wind is generated in the lower frequency range, depending on the microphone type, angle and diaphragm size. He concluded that the microphone position needs to be off-axis to eliminate the unwanted wind noise effects, and an additional windshield can be used. His findings correlate to the investigations of sound ports in the present work.

2.3. Air jet stream

The most critical measurement issue is the formation of a velocity-caused air-jet stream. It is generated at the port outlet with high voltage levels. A highly directive air stream pattern is observed with slight variations of its form, dependent on the port geometry. The microphone diaphragm is excited by the high-velocity air stream, causing distortions below approximately 400 Hz. The exact frequency range depends on the used angle. Suppose the microphone is positioned in the high-velocity area. In that case, it presents an obstacle for the stream, causing additional distortions due to vorticity and eddy formation at the edges of the microphone aperture.

The 60° off-axis measurement from figure 2.5 indicates that at large off-axis angles, these disturbances disappear. Therefore, the 60° angle is used as a disturbance-free reference measurement. Figure 2.7 shows the frequency response difference between the 60° off-axis measurement and some exemplarily selected angle measurements with decreasing relative angle alpha, for all four ports, with and without a windshield, at 1 Vrms.

These investigations show that wind noise decreases with an increasing off-axis angle. The low-frequency disturbances are neglectable after an angle of 35°. At this angle, the difference to the assumable disturbance-free 60° measurement is less than ± 2 dB. It is also revealed that using a windshield close to on-axis positions increases the measurement quality, damping the

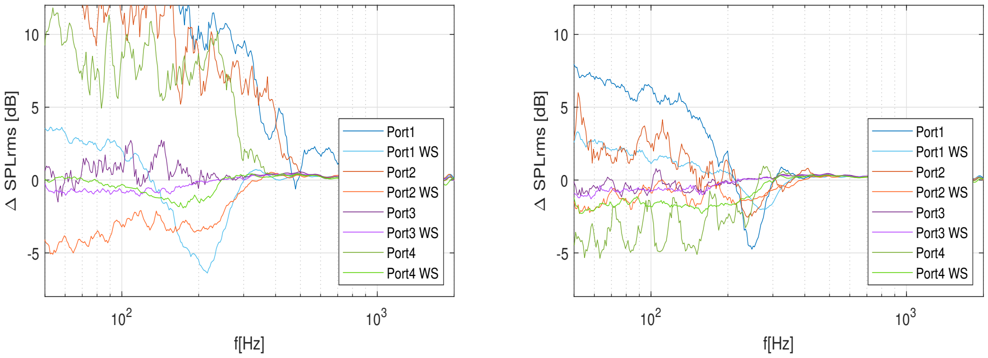

(a) 0°- 60°

(b) 20°- 60°

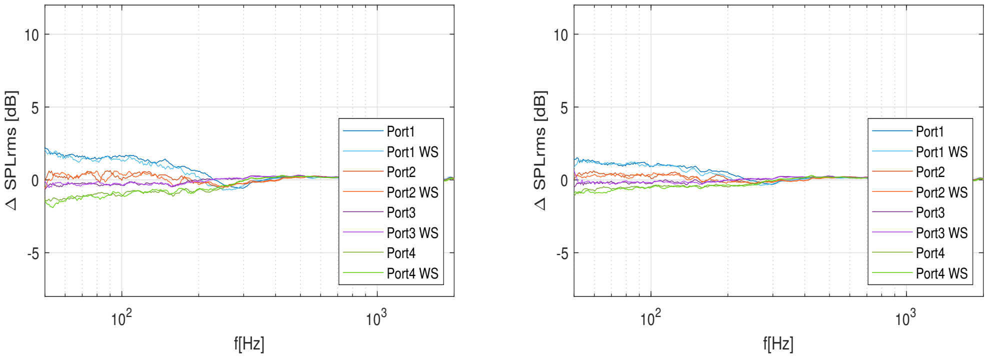

(c) 35°- 60°

(d) 40°- 60°

Figure 2.7.: Decreasing air jet stream distortions over angle at 1 Vrms (consecutive SPL difference to 60° off axis reference)

low-frequency distortions. With sufficient off-axis angle, the measurements with and without the windshield are nearly the same - the windshield shows no further improvement. Interestingly, the unsymmetrical, funnel-shaped SP03 seems to cause less unwanted blowing wind effects than the others - even at the on-axis measurement. The figures in appendix C show waterfall diagrams for the evolution of wind noise for all investigated angles and windshield applications. The SPL difference shown in appendix C uses the same calculation method mentioned above with the off-axis angle at 60° as a disturbance free reference.

2.4. Angle dependent high-frequency damping

Every loudspeaker system is collimated to higher frequencies. Similar behaviour is observed for sound ports. The port is assumed to act as an acoustic point source, with the rest of the system being its driver. Additionally, the on-axis position is considered a reliable reference without any high-frequency damping due to directivity. In figure 2.8(a), the angle-dependent damping is shown in the FRF of SP01 above 10 kHz. Figure 2.8(b) displays the maximum SPL difference above 10 kHz for all ports with and without windshield over angle.

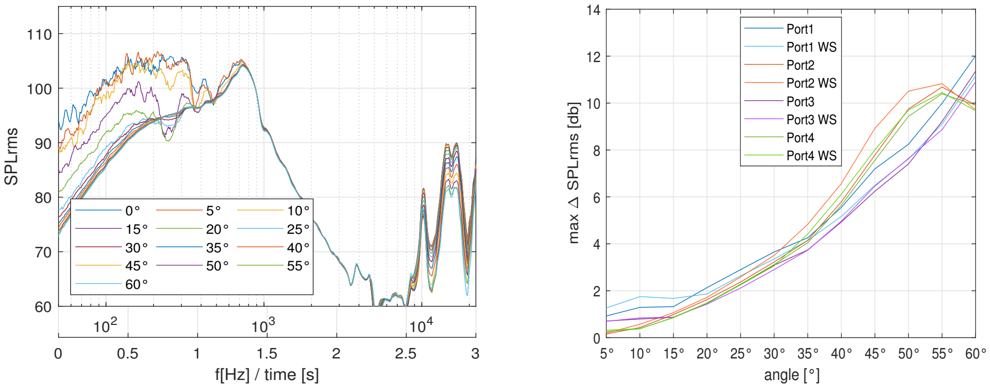

(a) FRF of SP01 at 1 Vrms (visible damping with increasing angle above 10 kHz)

(b) Maximum SPL difference above 10 kHz to the on-axis measurement over increasing off-axis angle

Figure 2.8.: Damping over angle at high frequencies (f > 10 kHz)

The angle-dependent damping starts above 4 kHz and increases with the off-axis angle. The most noticeable difference occurs at the port resonance frequency $f_{\frac{\lambda}{2}}$ around 17 kHz. The exponentially shaped ports (SP02, SP04) have little damping for small off-axis angles, but above 40° off-axis angle, the damping increase more rapidly for SP02 and SP04 than for the straight and funnel-shaped ports (SP01, SP03). The windshield does not influence the relative differences much but increases the overall damping at high frequencies - investigated in more detail in the following section. The general angle dependency for all ports is approximately 1 dB /5°.

Although a maximum SPL difference between on- and off-axis measurements up to 10 - 12 dB can be reached at high frequencies, the relative SPL between ports stay approximately the same. The angle dependency needs to be kept in mind for interpreting absolute values, but no compensations with, e.g. an equaliser, is necessary for the high-frequency damping. An overview of the angle-dependent high-frequency damping for all ports is presented in appendix B.

2.5. Windshield

Brixen in 2006 [Bri06] also showed that using a windshield can reduce wind noise at low frequencies up to 30 dB. In the previous sections, it was observed that the windshield increases the stability against unwanted blowing noise. It also was indicated that if used, some high-frequency damping occurs. The windshield is built from Basotech absorber material with a quarter-inch hole drilled in the middle of the 1 *x* 1 *x* 2 cm cube. In this section, the FRF of the windshield and the repeatability of its mounting are investigated. First, the FRF of the windshield is measured. A three-way, full-range speaker system is used with a sweep excitation at 1 Vrms and an angle of 30° at 3 cm distance for the microphone position. To accurately

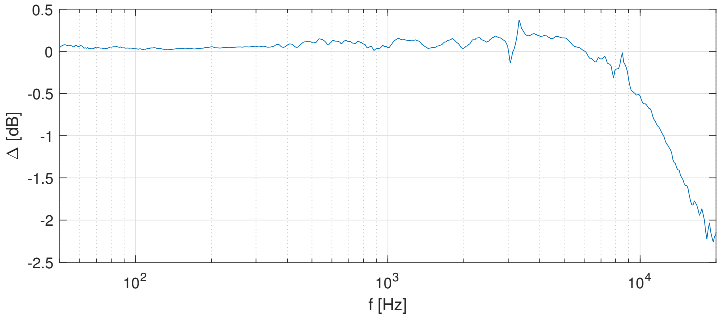

Figure 2.9.: Frequency response for the Basotech windshield

measure the frequency response with and without the windshield, the mean of four repetitions is used for each assembly to avoid potential measurement errors. The two remaining frequency responses are deconvolved to calculate the transfer function (FRF). Figure 2.9 shows the FRF of the windshield. Surprisingly, the windshield is almost linear below 8 kHz and acts as a low pass filter (LP) with -2 dB /octave (-6 dB /dec) above. The neglectable amplitude increase of 0.1 dB is assumed to derive from the "virtually" closer microphone position due to the attached windshield onto the microphone capsule or the area increase from quarter-inch microphone diameter to 1 cm windshield diameter.

Although the windshield has a relatively flat FRF, the mounting and remounting could tamper with the results. Therefore, another investigation is performed, measuring the mounting repeatability. First, the measurement variance is investigated by performing eight repetitive measurements without changing the setup, leading to a variance of ± 0.5 dB at low frequencies. Then the windshield is remounted four times correctly and five times poorly, which means it is mounted half the way on the microphone. For measurement nine (orange line), it is nearly falling off. Differences in the mean of the variance measurements are presented in figure 2.10. For the first four measurements with careful remounting, the observed difference is below ± 1 dB, but it is significantly higher for the poorly mounted cases. Following, using a windshield is reproducible, but mounting accuracy is substantial.

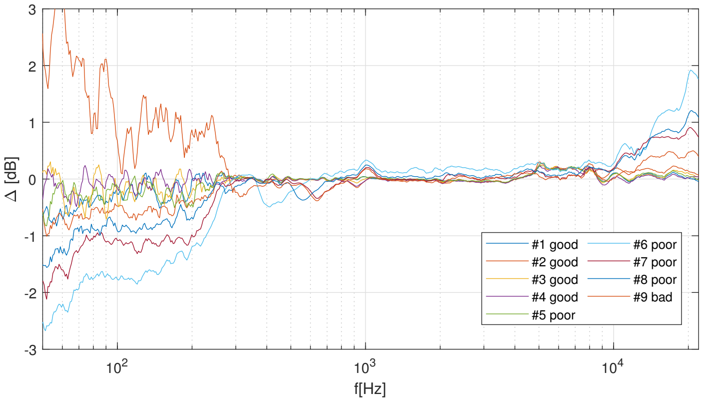

Figure 2.10.: Remounting repeatability of the wind shield (difference to static mount)

2.6. Conclusions of measurement (analysis)

The best measurement position is a trade-off between unwanted wind noise and angle dependency. Distortions caused by the air jet streams are neglectable after 40° off-axis angle. The use of a windshield additionally increases the general stability against unwanted wind noise with no considerable disadvantages. Merely, a soft low-pass characteristic above 8 kHz is caused by the windshield. The favourable position at 3 cm radius presents a good SNR while preventing the air-jet stream effect. Up to 40°, angle dependencies show a maximum difference of 7 dB for high-frequency damping but do not corrupt relative results. Therefore, the angle dependency does not need compensation. Finally, the best measurement position is found at a distance of **3cm with a microphone angle of** 40° **and a windshield** for additional stability. This setup is used for all further measurements.

3. Post processing and data analysis

Ultimately, the above-defined best measurement position and overall setup can investigate port noise without additional measurement distortions. The following chapter introduces the methods for separating the harmonic and non-harmonic signal parts, representing the measured noise in the time and frequency domain, and finally, calculating a parameter set for noise classification.

3.1. Vold Kalman Filter theory

A Vold-Kalman Filter (VKF) separates the signal into harmonic and non-harmonic components. Introduced by Håvard Vold and Jan Leuridan in 1993 [HL95], it is a heterodyne filter for tracking the sinusoidal components of a noisy signal. It can extract non-stationary features (the residual) from a signal using the known excitation frequency vector, e.g. a sweep. Formulated in a least-squares sense, the VKF solves a sparse linear system. The VKF minimises a cost function based on a structural and data equation like the Kalman filter. In the present work, the practical MATLAB implementation by Maarten van der Seijs is used [Sei21]. It is the second generation VKF with the ability to extract multiple harmonics simultaneously, with energy spreading in case of crossing harmonics. The Preconditioned Conjugate Gradient (PCG) algorithm presented in [FH00] is the base for the implementation. Tuma in [Tum05] shows the proper determination of the VKF settings.

"*The basic idea behind the Vold-Kalman filter is to define local constraints,* which *state that the unknown complex envelopes are smooth and that the sum of the* harmonics *should approximate the total measured signal. The smoothness condition is called the structural equation, and the relationship with the measured data is called the data equation.*" [Gad+99] The data and structural equations define the filter as:

$$\mathbf{y} = \mathbf{x}e^{\mathrm{j}\Theta} + \boldsymbol{\eta} \tag{3.1}$$

$$\nabla^2 x_n = x_n - 2x_{n-1} + x_{n-2} = \varepsilon_n \tag{3.2}$$

The data equation 3.1 describes the measured signal $\mathbf{y}$ as a sum of tracked complex envelopes $\mathbf{x}$, modulated by a rotating phasor Θ and the additional noise $\boldsymbol{\eta}$. The rotating phasor is the integral of the tracked frequency f_c with respect to the sampling frequency f_s.

$$\Theta(n) = \sum_{i=0}^{n} \frac{2\pi}{f_\mathrm{s}} f_\mathrm{c}(i) \ . \tag{3.3}$$

The structural equation 3.2 specifies smoothness of adjacent samples within the tracked component. In this case, a 2^{nd} order filter with N samples is denoted. Rewriting the data and structural equation in matrix notation follows

$$\mathbf{y} = \begin{bmatrix} x(1) \\ \dots \\ x(N) \end{bmatrix} \begin{bmatrix} e^{\mathrm{j}\Theta(1)} & 0 & 0 \\ 0 & \dots & 0 \\ 0 & 0 & e^{\mathrm{j}\Theta(N)} \end{bmatrix} + \begin{bmatrix} \eta(1) \\ \dots \\ \eta(N) \end{bmatrix} \tag{3.4}$$

and

$$\nabla^2 \mathbf{x_n} = \begin{bmatrix} 1 & -2 & 1 & \dots & 0 & 0 & 0 \\ \dots & \dots & \dots & \dots & \dots & \dots & \dots \\ \dots & \dots & \dots & \dots & 1 & -2 & 1 \end{bmatrix} \begin{bmatrix} x(1) \\ \dots \\ x(N-2) \end{bmatrix} = \begin{bmatrix} \varepsilon(3) \\ \dots \\ \varepsilon(N) \end{bmatrix} \tag{3.5}$$

Or written in short form

$$\mathbf{y} = \mathbf{x}\mathbf{C} + \boldsymbol{\eta} \tag{3.6}$$

and

$$\nabla^2 \mathbf{x_n} = \mathbf{A}\mathbf{x} = \boldsymbol{\varepsilon} \tag{3.7}$$

with $\mathbf{C}$ being a diagonal matrix which elements are the signal phase samples. Matrix $\mathbf{A}$ contains the elements of structure equation 3.2 along its main diagonal. Three data samples are recursively fitted at a time for a two-pole filter. For a general order of p the adaptive filter uses p + 1 samples for the recursion.

The filter result, as output envelope **x**, is given by minimizing the error terms η and ϵ. Following, the system equation is denoted as,

$$\mathbf{x} = \left(\mathbf{A}^T\mathbf{R}^T\mathbf{R}\mathbf{A} + \mathbf{E}\right)^{-1}\mathbf{C}^H\mathbf{y} \tag{3.8}$$

where **E** is the identity matrix and H powered denotes the conjugate transpose. Tuning of the filter for simultaneous envelopes (harmonics) is performed by a square matrix **R** with weighting factors at its main diagonal. A higher rating factor r leads to narrower bandwidths. [Kun+18]

When several harmonics are estimated simultaneously, the data equation ensures the distribution of the total signal energy over all harmonics. Evaluation of simultaneous harmonics is based on an iterative approach, the Preconditioned Conjugate Gradient (PCG) algorithm [FH00]. Together with the smoothness conditions of the structural equation, this enforces a decoupling of close and crossing harmonics. Decoupling is significant for acoustic applications, where harmonic crossings cause beating and disturbing roughness.

In other words, the harmonics may be regarded as amplitude and phase-modulated carrier waves that vary in frequency. Using heterodyne filtering in the VKF shifts the k-th harmonic to the DC frequency range and then low pass filters it. The Vold-Kalman filtration includes a simultaneous envelope detection of both magnitude and phase. Subsequently, remodulating the k-th complex harmonic by the fundamental carrier frequency gives the time signal for each harmonic. A significant advantage of this filtering is that the harmonics extracted as waveforms have no phase bias (time delay).

Non-real time processing and the necessity of some prior knowledge about the excitation frequency vector are the only disadvantages of the VKF.

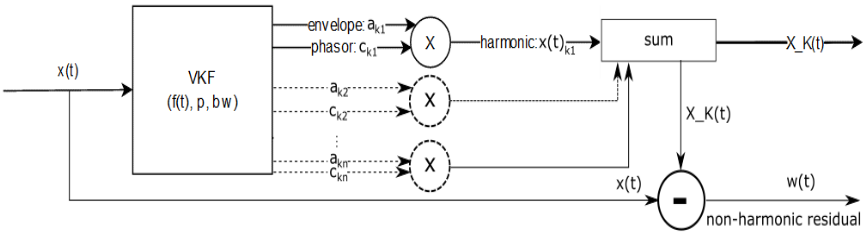

Figure 3.1.: VKF block diagram

3.2. Vold Kalman Filter example

Next, a typical example of the specific VKF used in this work is presented. Port noise is known to be chaotic and time-invariant. It is assumed that only the non-harmonic components of the measurements contain port noise. Figure 3.1 shows a block diagram of for a VKF with $x(t)$ being the microphone signal, $f(t)$ denotes the excitation frequency vector, p is the filter order, bw denotes the bandwidth of the filter, a_k is the complex envelope and c_k being the phasor with the subindex $_k$ denoting the k-th harmonic. The signal is split into its harmonic $X_{K(t)}$ and non-harmonic parts, resulting in a time-domain waveform x_k for each k-th harmonic and the port noise residual $w(t)$. This residual is analysed more thoroughly, defining a fingerprint for port noise in section 4.

Figure 3.2 shows the power spectrum of the original measurement and a filtered residual microphone signal for port four. The excitation is a logarithmic three-second long sweep from 50 Hz to 20 kHz with 3.15 Vrms. Broadband noise between 0.5 and 1.5 seconds of the excitation and the harmonic structure of the measurement are displayed. After filtering, only the non-harmonic parts remain in the residuum. The figure shows the power spectrum at a particular excitation frequency. A second axis shows the frequency excitation time instance for better orientation.

The extraction of the first 12 harmonics showed good performance for all ports. An order of $p = 2$ and a variable bandwidth bw relative to the fundamental frequency is used. Although, every filter order increases the

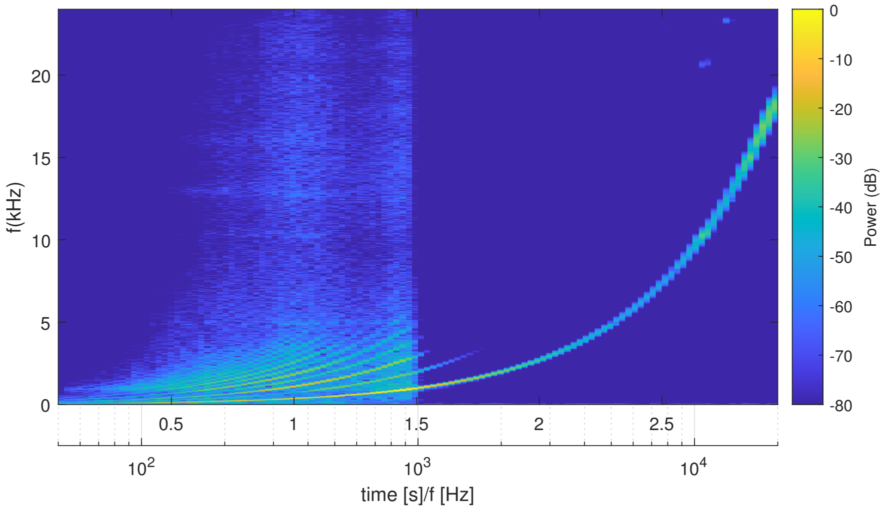

(a) Original unfiltered microphone signal with sweep excitation, harmonics and noise

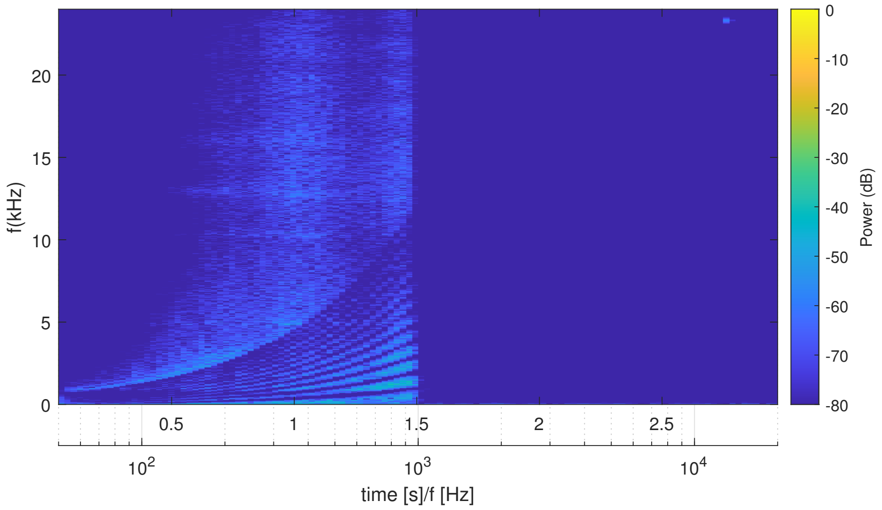

(b) Residual after VKF, only non-harmonic noise components left

Figure 3.2.: Power spectrum of the original and residual signal at 3.15 Vrms with a frequency resolution of 25 Hz

roll-off factor by -40 dB per decade, a second VKF instance is needed to remove the fundamental from the residual totally. The second instance is solely used for the fundamental f_0 and is implemented as a second stage serial cascade after the first filter. In figure 3.2 some frequency content in the residual after 2.5 seconds and above 10 kHz is still visible, but these effects arise from artefacts of the visualisation. For all sweep measurements, the variable bandwidth is defined as:

$$\mathrm{bw} = \begin{cases} 5\text{ Hz - }400\text{ Hz} & \text{for } 50\text{ Hz} \leq f_{sweep} \leq 1\text{ kHz} \\ 400\text{ Hz - }1\text{ kHz} & \text{for } 1\text{ kHz} \leq f_{sweep} \leq 20\text{ kHz} \end{cases} \tag{3.9}$$

Setting the VKF parameters strongly influences the algorithm's performance and needs to be tested individually, depending on the specific measurement requirements. More on the selection of the filter bandwidth and VKF parameters can be found in [Tum05].

3.3. Frequency domain

Figure 3.3 shows the spectrograms for all four sound ports during a three-second long exponential sweep excitation with the highest investigated voltage step at 3.15 Vrms. The plots show non-harmonic distortions in the upper-frequency range above 4 kHz. Different port geometries cause small and broadband noise over a wide frequency range. Above 1 kHz (after 1.5 s), the signal power of the whole system decreases, and neither harmonic nor non-harmonic distortions remain, only the sweep excitation is present.

Compared to the velocity measurements of figure 2.4, the spectrograms also show frequency dependency of port noise coupled with the velocity at the driver membrane. Still, the driver velocity is not the only cause for the noise. The spread of the broadband noise in, e.g. SP02, between its first and second resonance peak is larger than the driver-velocity would indicate. Distortions in SP01 and SP03 are also more constant over the lower frequency range than one would expect from the driver cone velocity measurements.

The author suggests thinking of port noise as a superposition of different noise sources emerging in the ports at various stages, depending on the port

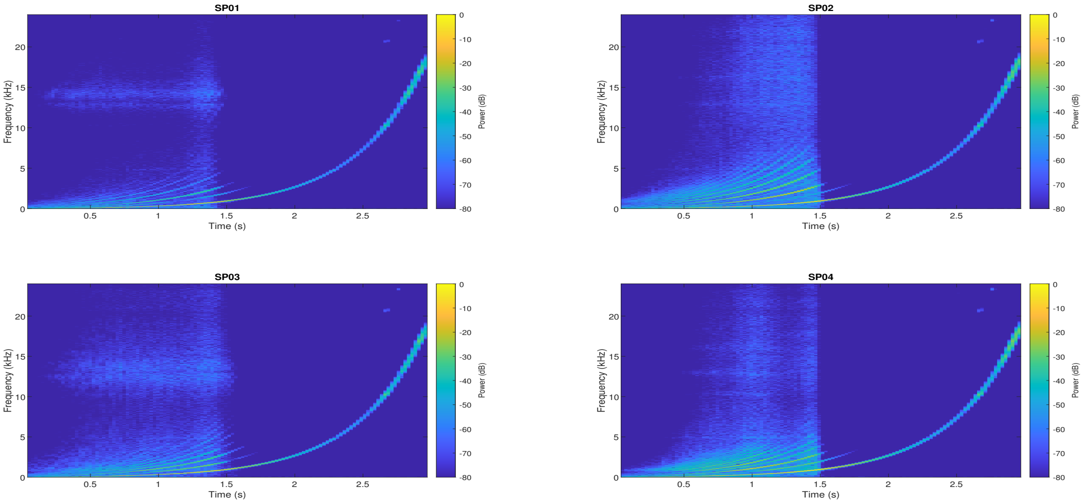

Figure 3.3.: Spectrogram of a three-second long sweep with 3.15 Vrms in dBFS for all four sound ports (50-20 kHz)

geometry. These noise sources then propagate through the speaker system and are further enhanced by the system's response. Meaning that the exact position of an emerging noise source significantly influences whether it is amplified afterwards or not:

"Noise sources at the inlet of a port will be stronger frequency shaped than sources at the outlet."

Depending on the port geometry, the spectrograms of figure 3.4 also show different harmonic structures. The asymmetric sound port SP03 shows even and odd number harmonic distortions like a sawtooth wave. The symmetric sound ports SP01, SP02 and SP04 have mainly odd-harmonic distortions. Moreover, the exponential shape of ports SP02 and SP04 amplify the odd harmonic structure stronger, resulting in a solid third and fifth harmonic, causing more THD.

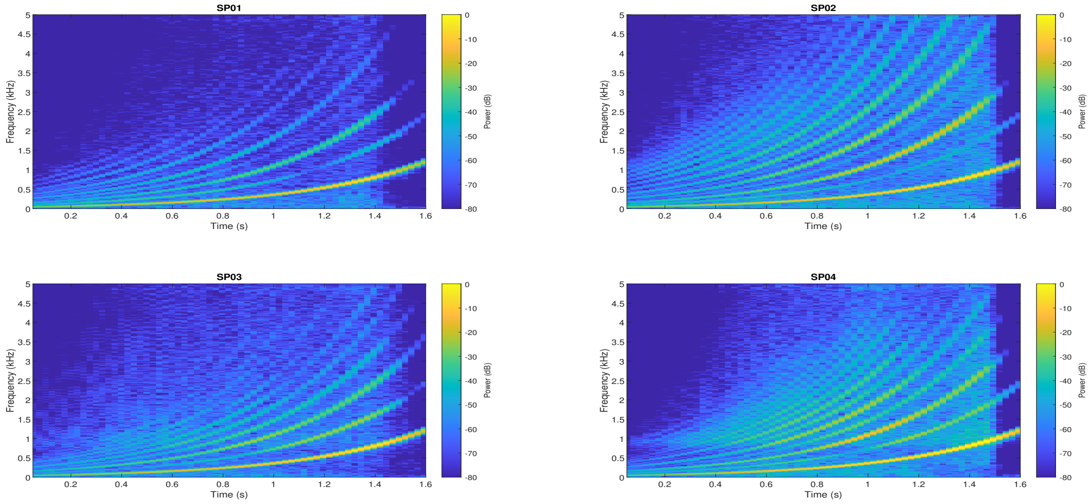

Figure 3.4.: Spectrogram, zoom on harmonic structure

3.4. Time domain

Next, the analysis in the time domain provides a better understanding of the evolution of port noise. Turbulent airflow is not stationary, but if the system is excited with a sinus wave, the produced broadband noise has some periodic structure.

Time signal measurements with a laser vibrometer at the speaker cone show the port's backlash (acoustic load) on the speaker, causing harmonic distortions at the driver cone. These distortions at the very input of the system contribute to the noise quality but are not port noise itself, emphasising the analysis of the non-harmonic distortions with, e.g., the VKF. On the contrary, the pressure microphones in the cavity and nearfield reveal distinct periodic distortions at the rising and falling slope of the sine tone excitation, depending on the port shape, indicating noise. The measurement signal was a 100 Hz sinusoidal tone with a length of 3 s for the microphone signals and 8 ms for the laser vibrometer. As mentioned before, at 100 Hz, all ports have approximately the same input velocity and therefore are comparable.

Harmonic distortions

First, the contribution of harmonic distortions is investigated. The manufacture specification for maximum linear excursion of the two-inch driver is 1.7 mm at its resonance peak. For measurements with an open front volume (without a port), the maximum excursion is 0.47 mm at 100 Hz. The maximum excursion for measurements with sound ports is lower, as shown in table 3.1.

port/condition:	SP01	SP02	SP03	SP04	open front volume
max. excursion [mm]:	0.34	0.37	0.40	0.43	0.47

Table 3.1.: Maximum driver excursion for the open- and investigated ports (3.15 Vrms)

Due to the high Q-factor of the driver speaker, harmonic distortions at the cone will occur at higher amplitudes. Figure 3.5 shows the spectrum of the calculated excursion and the structure of the harmonic distortion from the vibrometer measurement with an open front volume at the maximum amplitude investigated (3.15 Vrms). The THD calculated from the driver excursion is approximately 4% (-27 dB). Adding a port changes the structure of the harmonics drastically and increases the THD up to 40%. Figure 3.6

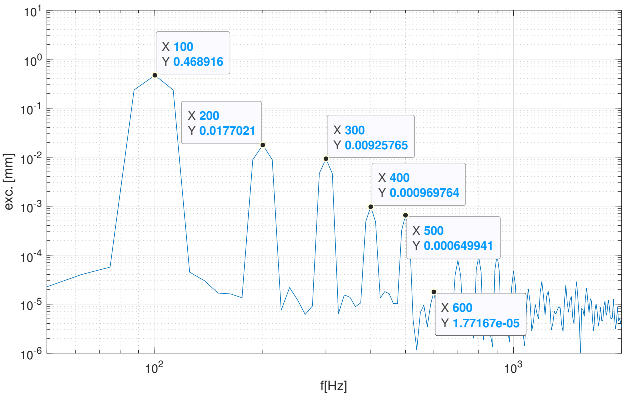

Figure 3.5.: Spectrum of the driver cone excursion measurement for open front volume with a sinus tone of 100 Hz at 3.15 Vrms resulting in 4% THD (FFT with 2048 samples and hanning window)

shows the velocity at the driver speaker with open front volume over increasing voltage. No distinct distortions of the sine wave are visible (very little at the highest step).

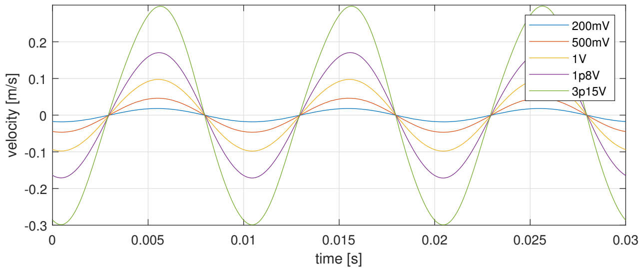

Figure 3.6.: Velocity measurement for an open front volume (no port)

Compared to the open front volume measurements, figure 3.7 shows harmonic distortions of the driver velocity caused by the ports. These measurements demonstrate the backlash of the acoustic mass and added air

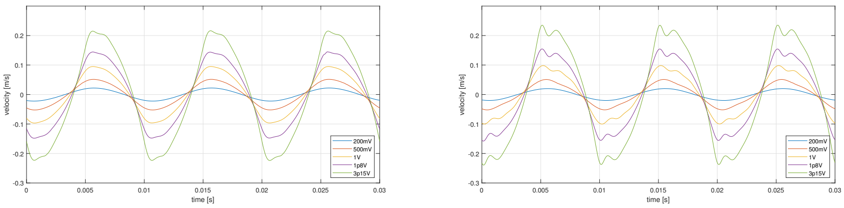

(a) SP01 (b) SP02

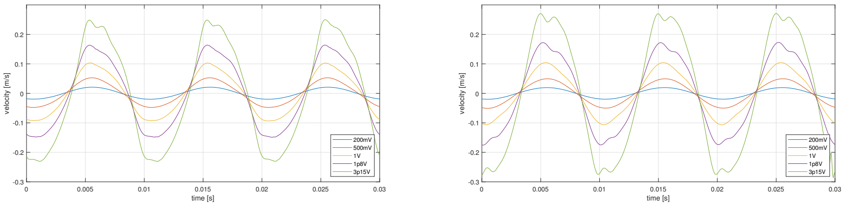

(c) SP03 (d) SP04

Figure 3.7.: Velocity measurement for all ports with increasing driver voltage. Harmonic distortions occur at the driver membrane at maximum velocity (excursion = 0)

stiffness of the port to the driver membrane. Following, the separation of the harmonic and non-harmonic components is crucial to measure port noise correctly.

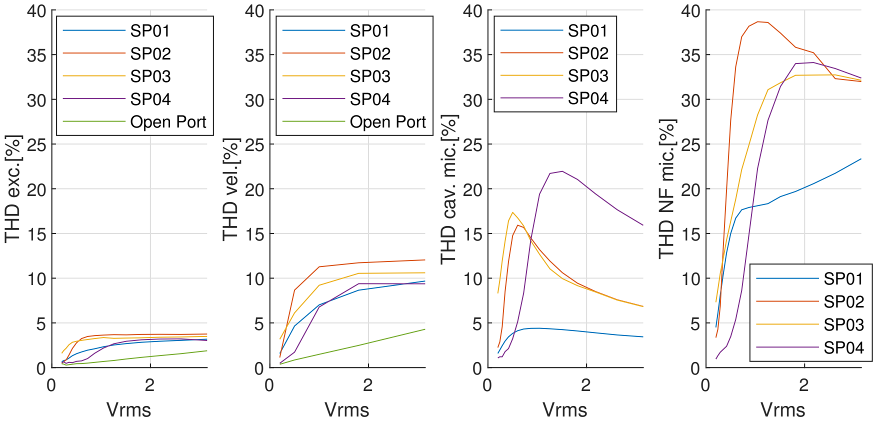

Figure 3.8.: The evolution of harmonic distortions throughout the speaker system

The first subplot of figure 3.8 shows the harmonic distortion increase from open front volume excursion measurements (green line, THD = 4% at 3.15 Vrms) to measurements with ports. The second displays an introduced THD of more than *10* % in the velocity of the driver cone with added ports. The following two subplots show the evolution of harmonic distortions throughout the acoustic system, reaching a THD up to 40%. A vast amount of harmonic distortions will rise from the acoustic load of the port on the driver cone rather than from turbulent airflow. In the end, a good loudspeaker should have minimum distortion overall.

Non-harmonic distortions (NHD)

Next, the contribution of non-harmonic distortions is investigated in the time domain, especially the occurring periodic structure during the inflow and outflow of air in the port. Figure 3.9 shows a step by step investigation of non-harmonic distortions of the pressure microphone in the nearfield outside the ports. The top subplot shows the unprocessed microphone

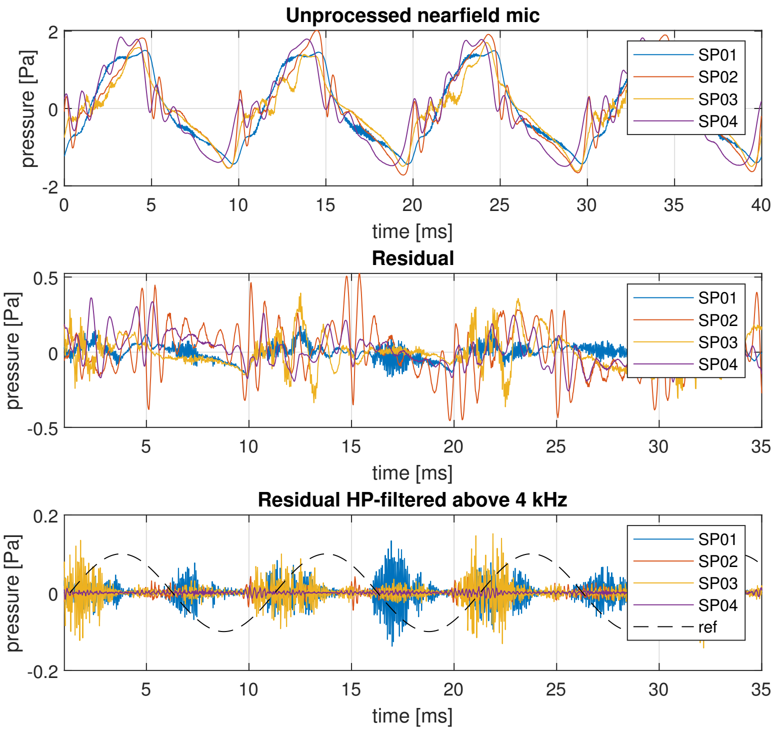

Figure 3.9.: Noise filtered first with VKF and then HP-filter above 4 kHz (calculation steps for the NHD parameter)

signal. The residual noise after VK filtering is shown in the middle plane. In the bottom subplot, an additional high-pass filter above 4 kHz reveals the periodic structure of the emerging noise. The dashed line in the bottom subplot indicates a reference to the 100 Hz sine excitation. It was time aligned with a lag of 62 samples. ($fs = 44.1$ kHz)

When compared, the ports in figure 3.10 show interesting behaviours during each excitation period. The straight port SP01 generates noise both for the outwards and inwards movement of air. In comparison, the funnel-shaped asymmetric sound port SP03 mainly generates noise while air streams out. SP02 and SP04 are symmetrical in the direction of propagation, with an exponential decreasing and increasing port shape. Both produce moderate

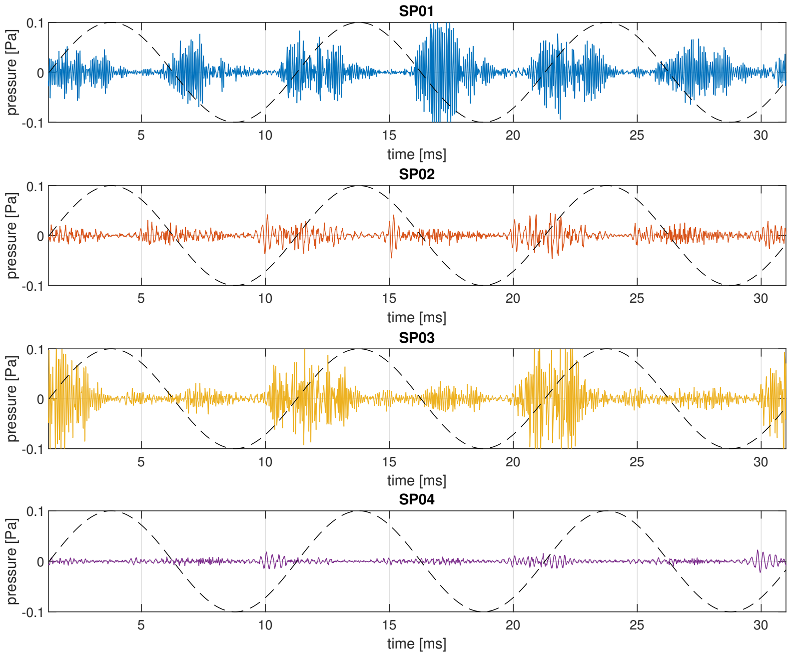

Figure 3.10.: Port noise periodicity while sine excitation with 100 Hz and 3 Vrms

noise levels at the frequency of 100 Hz. A new parameter for detecting non-harmonic distortions (NHD) is introduced and defined as,

$$NHD = HPF(VKF(x(t))) \tag{3.10}$$

with HPF indicating the high pass filter, VKF indicating the used Volt Kalman filter and $x(t)$ being the measured pressure signal from a near field microphone.

Analyzing time over a wide frequency range and multiple voltage levels is not suitable for engineering. The following section (3.5) deals with defining a parametric representation for these findings over a more representative frequency range. The basic principle for a port noise indicator (NHD) is already shown here.

3.5. Analytic parameters

Over the last decades, standard parameters for analysing a speaker system's performance have been established and are used in measurement systems like the Audio Precision APx526, Klippel KA3 or Listen Inc. AmpConnect ISC. Existing parameters are the Thiele-Small-Parameter (TSP) for speaker designs, energy levels like the sound pressure level (SPL), distortion factors like the THD and HOHD (Higher Order Harmonic Distortion); or bandpass filter noise measures like Rubb and Buzz. The sound pressure level (SPL) and the THD parameter link the analysis to those standard acoustic evaluations in the present work. The energy ratio in the residual noise compared to the excitation energy (Noise to signal ratio or NSR for short) represent new analytic differences due to non-harmonic distortion (NHD) measurements and assumed air noise correlation.

The analytic parameters used in this work are calculated within a 3rd-octave band around the instantaneous sweep frequency: The system responses are divided into blocks. The logarithmic sweep excitation frequency changes during those blocks, but the relative change to the centre frequency (frequency supporting point) of each block is constant. Therefore a fixed block length of 4165 samples, corresponding to a 3rd-octave of the block's centre frequency, can be used. Frequencies below, around and slightly above the two velocity resonance peaks (see figure 2.4), i.e., at (100,200,400,600,800,900 Hz) show a good representation over the total frequency range. Parameters calculated over the sweep excitation's non-static third band frame are almost identical to parameters calculated from a static sine tone excitation at *100 Hz*. The third band analysis is assumed representative over the whole frequency range while ensuring robustness for the calculation method over time.

The following plots exemplify the sweep excitation around the third band of 100 Hz and the calculation method for each parameter over increasing voltage. Respective higher velocities then again increase the probability of air noise.

As mentioned above, the velocity at 100 Hz is nearly the same for all ports. It is assumed to be a fair comparison for port shape-driven effects. For other factors like the overall loudness or the amount of distortion, the comparison at 100 Hz might not be representative. Drawn conclusions on port behavioural trends are therefore validated over the entire frequency range. Appendix D shows a detailed comparison of all parameters at the defined frequency supporting points.

Sound pressure level

The following sound pressure levels (SPL) represent the calculated root mean square (rms) voltage values of the pressure microphone signal p measured over a short signal window (4156 samples) equally to a 3rd-octave band in reference to the threshold of hearing $p_0 = 20$ µPa.

$$SPL = 20 * log(\frac{rms(p)}{p_0}) \tag{3.11}$$

Slight differences between the SPL in previous sections and those calculated here arise from using two different measurement systems over time. Initial measurements (section 2.1) were performed with the Sound Solutions

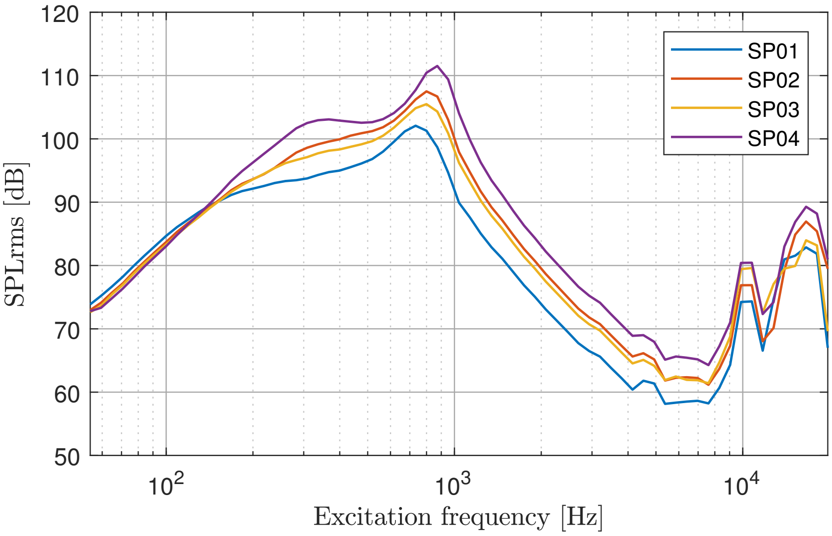

Figure 3.11.: Sound Pressure Level calculated from 1/3-octave band windowed RMS pressure values at 1 Vrms excitation

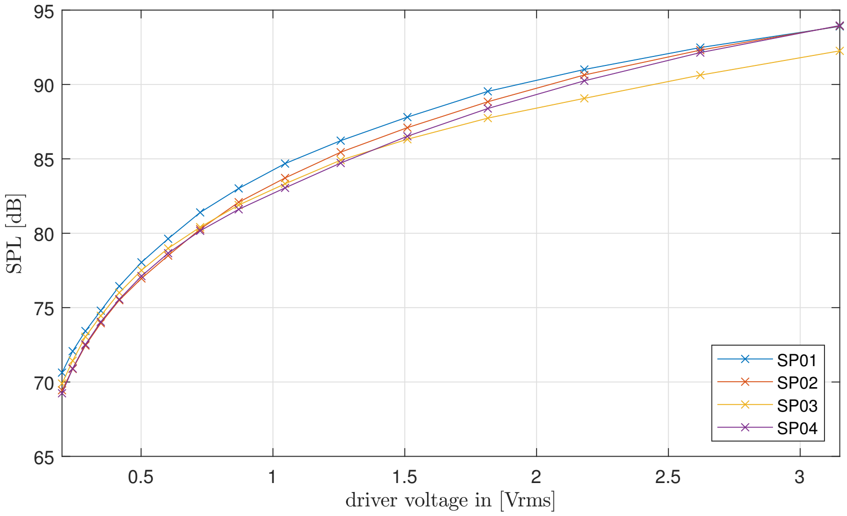

Figure 3.12.: Sound Pressure Level calculated around 1/3-octave band of 100 Hz excitation over increasing driver voltage

internal software "AMS". All later data acquisition was performed with the Audio Precision APx526 multichannel audio analyser as described in chapter 2. The post-processing is solely done in MATLAB. SPL differences to e.g. figure 2.5(b) are minor and mainly caused by the 3rd-band averaging. Relative differences between the ports stay valid.

Figure 3.12 shows the calculated SPLrms values over several amplitude steps evaluated at a 3rd-octave band around 100 Hz. The relative level differences between ports change with rising driver levels due to compression effects and an increasing influence of turbulences. Those differences are additionally velocity- and, therefore, frequency-dependent. The comparison between the port's sound pressure levels shows that the relative level differences are crucial for a fair noise comparison and need to be considered for further parameter calculations.

Evaluated over the selected frequency supporting points, the straight port SP01 tends to produce much lower SPL than the others, and SP04, with the largest diameter, is the loudest. In the appendix figure, D.1 shows the SPL at the defined frequency supporting points.

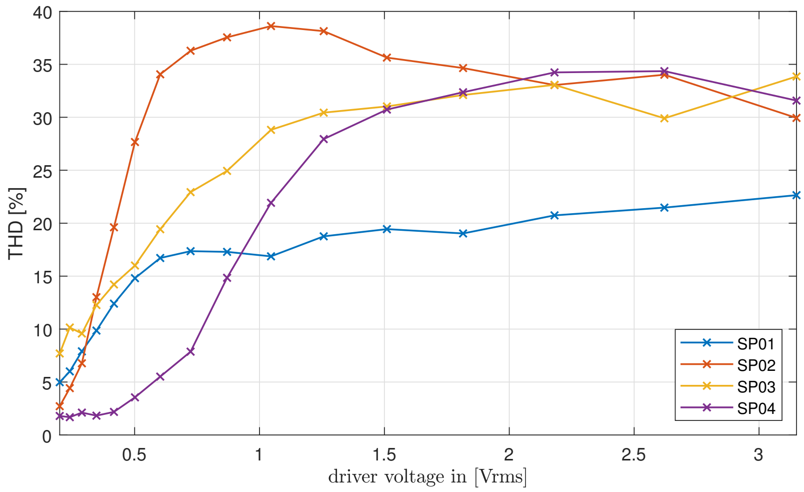

Figure 3.13.: THD calculated around 1/3-octave band of 100 Hz excitation over increasing driver voltage

Total harmonic distortion

The total harmonic distortion (THD) is defined by the power ratio of the fundamental k_1 and the first five harmonics, k_{2-6}.

$$THD_{\%} = \frac{\sqrt{k_2^2 + k_3^2 + k_4^2 + k_5^2 + k_6^2}}{k_1} \cdot 100 \tag{3.12}$$

The definition is simple, but the extraction of harmonic components is not a trivial task. One could use multiple techniques, for example, calculating a periodogram with peak detection (see Matlab implementation [MAT22a]), the Farina method for swept-sine excitation signals [Far00] or the VKF shown in section 3.1. A rough comparison between the different methods yields differences up to 10% for THD.

This work used the Matlab implementation which *returns the total harmonic distortion (THD) in dBc of the real-valued sinusoidal signal x. The total harmonic distortion is determined from the fundamental frequency and the first five harmonics using a modified periodogram of the same length as the input signal.* (4165 samples) *The modified periodogram uses a Kaiser window with $\beta = 38$.* [MAT22a]).

The MATLAB implementation showed similar results in comparison to measurements with the Audio Precision APx526 measurement system. The calculated THD values in dB were expressed in % in the present work.

Figure 3.5 shows an example for the chosen approach. The THD calculated around a 1/3-octave band of the 100 Hz sweep excitation shows differences between the ports, but like for the SLP parameter, the results are highly frequency dependent. Still, over the whole frequency range, a trend for sound ports with exponential shapes having more THD is found, as shown in the appendix in figure D.2.

Residual port noise energy

The residual signal after the VKF only contains non-harmonic distortions, consisting of a deterministic part, i.e. shaping caused by port resonances and a stochastic part like air noise. The signal to noise ratio (SNR) also strongly influences the quality of the residual. Air noise in micro-speaker systems has either a high-frequency small band or broadband noise shape. An additional high pass filtering stage increases the SNR and separates other failure modes from air noise.

Non-deterministic periodic structures during each excitation period are good air noise indicators. Other typical noisy failure modes in micro-speaker systems, like membrane buckling, wire loop hitting, or some rattling, are nearly always deterministic. Such failure modes happen at sudden distinct moments in time, correlated to large membrane displacements, but not over a more extended period. On the other hand, turbulent airflow needs some time to establish and collapse eddies. During the time signal analysis (section 3.4: figure 3.9 and 3.10) the emergence of non-harmonic distortions (NHD) was shown in detail for a sinusoidal tone with 100 Hz. With the same approach as shown in section 3.4 now a more general solution is presented.

Figure 3.14 shows the rising non-harmonic distortions (NHD) over increasing driver voltage for all ports around 100 Hz sweep excitation in dB. Compared to the THD curve in the previous paragraph, a certain level is needed for NHD to rise above the noise floor and get measurable. Still, this noise might not be audible because it is masked by the fundamental. Additional, a port producing less noise might also have an overall lower SPL,

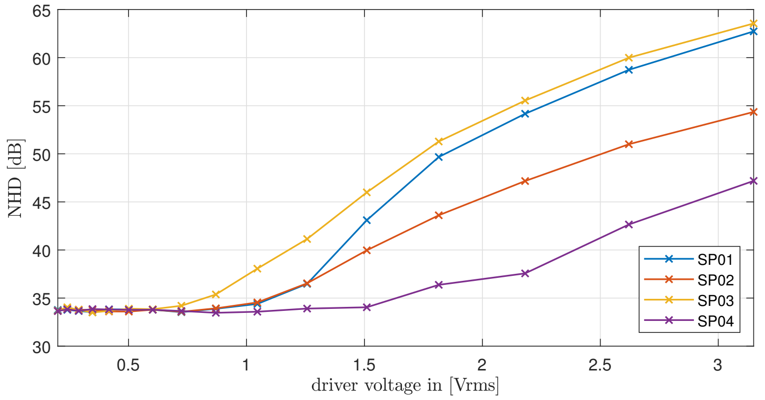

Figure 3.14.: Non-harmonic distortion (NHD) calculated around 1/3-octave band of 100 Hz excitation over increasing driver voltage

which makes rating sound ports difficult. Therefore, the NHD is normalised to the total SPL, as shown in figure 3.15. The *dBr* value indicates the noise to signal ratio (NSR). High normalised NHD at low driver voltages show

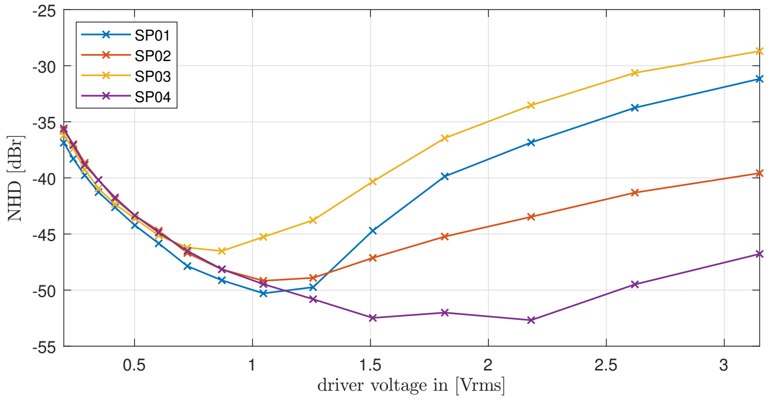

Figure 3.15.: Normalised non-harmonic distortion (nNHD)

bad SNR. At a certain driver voltage (∼ 0.7 Vrms) the SNR increase gets lower than the NHD increase, and the NHD values rise. This turning point is dependent on the sound port geometry and might be a good indicator of port performance, defining good performance by producing the highest SPL with minimum noise. The NHD curves also show that SP04 has the lowest noise at 100 Hz for high voltages, but not over the total frequency range. At 300 Hz and 400 Hz, SP01 has the lowest NHD. SP03 performs worst over the total frequency range for almost all driver voltages, as shown in figures D.3 and D.4 in the appendix.

Correlation to the Reynolds number

Additional, Reynolds number calculations correlate to the level for the onset of air noise for the 100 Hz sine tone measurement shown in figure 3.14. The driver membrane velocity was measured with the Polytech laser vibrometer. The velocity in the port is approximated as the velocity at the driver membrane S_d multiplied by the relation between the driver membrane area and port cross-section area S_0, assuming no loss in the front cavity of the speaker. The kinematic viscosity of air at 20° is $\nu = 1.15111 \cdot 10^{-5}\ \frac{m^2}{s}$ and the hydraulic diameter or characteristic length of the tube is approximated with the minimum inner diameter of the port. (see figure 2.2)

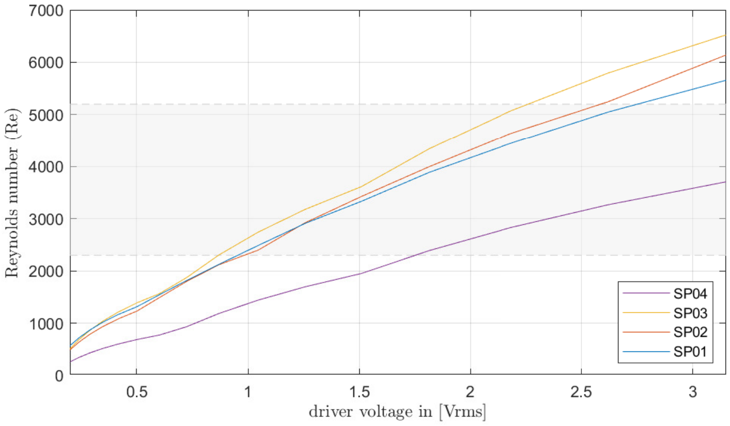

Figure 3.16.: Reynolds number approximation for a 100 Hz sinusoidal signal over increasing driver voltage (the grey area indicates the transition between laminar and turbulent air flow)

In figure 3.16 the grey area indicates the transition zone from laminar to turbulent flow. The necessary voltage level for the onset of turbulences correlates well to the onset of absolute NHD, except for the difference between SP01 and SP02. The straight port SP01 introduces more acoustic load on the driver membrane, producing less velocity in the port but causing significantly higher noise when measured with a near filed microphone. The exponential port SP02 shows the advantage of a flare at the inlet and outlet known from bass-reflex investigations.

3.6. Psychoacoustic parameters

Objective parameters are acceptable for detecting air noise, but they do not provide information about its quality. Psychoacoustic parameters cover the human perception of this noise. Listening to the residuals revealed multiple failure modes clear to the ear but difficult to quantify. Many questions came up: What is annoying to the ear? At which level is some noise audible? Are there multiple air noise types? If yes, how many? Performing a listening test for each loud speaker in mass production is unpracticable. A more thorough analysis and classification of air noise is possible with the psychoacoustic parameters, measured from a near filed microphone and calculated with a provided psychoacoustic MATLAB toolbox in [Son98]. Two sets of psychoacoustic parameters were calculated, one for the original signal and one for the residual signal.

Loudness level

The loudness level (LN) in phon is the subjective perception of a stimulus compared to a 1 kHz tone played at the same level. Like decibel, it is a comparative measure. At 1 kHz the phon and SPL scales are equal. The equal-loudness contours are a well-discussed topic in literature. Although outdated, the most famous example is the *Fletcher-Munson* curves [FM33], also known as the phon curves. All standard rated SPL like dB(A) are based on similar experiments. In this work, the calculation is defined as the standard from Zwicker in [Zwi+91].

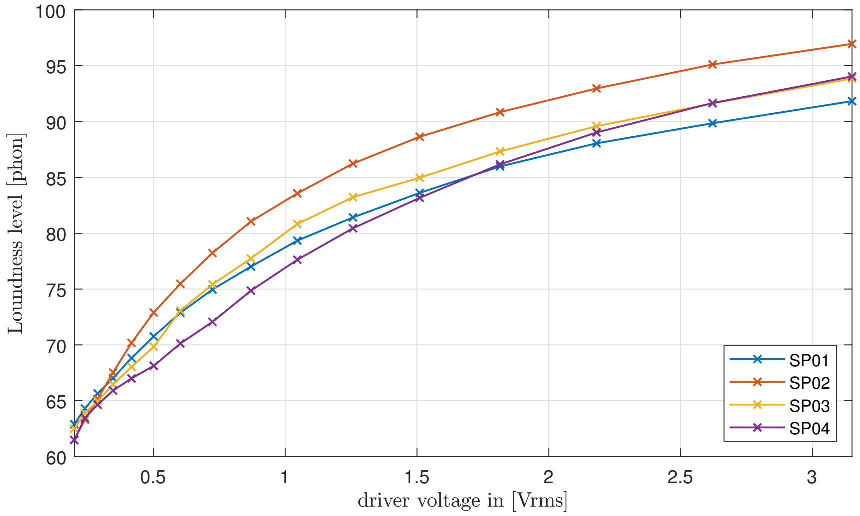

Figure 3.17.: Loudness level rating for the original signal calculated around an 1/3-octave band of 100 Hz excitation over increasing driver voltage

Over the whole frequency range, the trend for SP01 having the lowest level and SP04 being the loudest stays the same. The loudness level definition by Zwicker is assumed to be the most accurate. Therefore, only this level meter is shown in the appendix in figure D.5 and D.6 for both the residual and original signal.

Loudness

The perceptive rating over the frequency range is the same for the loudness (N) and the loudness level (LN), but with adapted scaling in the unit sone. The scaling was selected so that a change in volume perception by a certain factor numerically causes the same change in the loudness measure. If, for example, a 1 kHz sine tone with 40 dB(SPL) (LN = 40 phon, N = 1 sone) is increased by a factor of two, this results in an absolute sound pressure level of 50 dB(SPL) (LN = 50 phon) and loudness of N = 2 sone. The loudness measure directly represents how much louder a sound event is compared

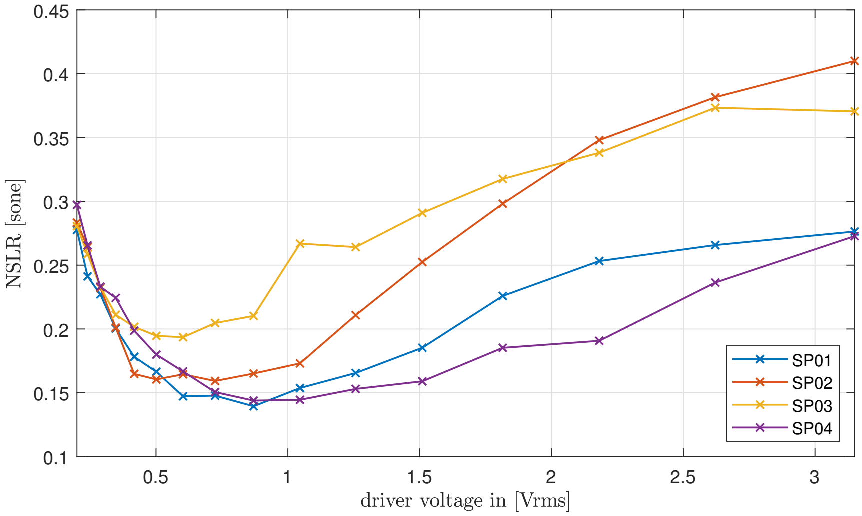

Figure 3.18.: Noise to signal loudness ratio (NSLR) over increasing driver voltage at the 1/3-octave band around 100 Hz (Loudness of the residual normalised with the loudness of the original signal)

to another. [Son98]

$$NSLR = \frac{N_{res}}{N_{sig}} \tag{3.13}$$

In equation 3.13, the loudness for the residual is normalised with the loudness of the original signal. This new loudness measure is called the noise to signal loudness ratio (NSLR) and is shown in figure 3.18. The NSLR is used in section 4 to rate the quality of port noise at different driver voltages and frequency support points.

Evaluated over the total frequency range, the loudness ratio reveals a possibility to perceptually rate ports on the noise they introduce, shown in the appendix in figure D.9. Also, the loudness of the original signal is up to five times higher than the noise in the residual.

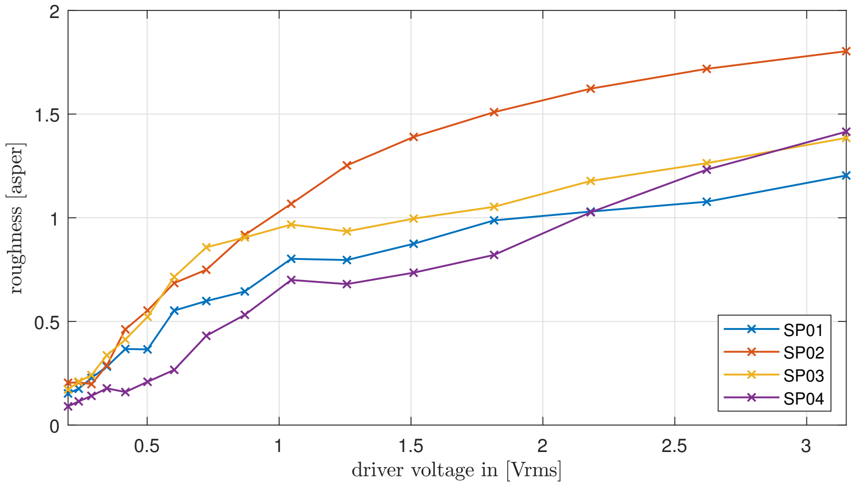

Figure 3.19.: Roughness of the original signal over increasing driver voltage at the 1/3-octave band around 100Hz

Roughness

Roughness is an elementary auditory sensation in psychoacoustics. [ZF13] It describes harsh sounds caused by frequency and amplitude modulations between 20 Hz to 300 Hz and is measured in the unit asper [Aur85]. A good example of how roughness is perceived is the presentation of two sine tones with the frequencies f_1 and f_2.

At the beginning, the level of f_2 equals f_1. The amplitude of f_2 slowly increases, resulting in a beating with $\Delta f = f_2 - f_1$. The perceived sound becomes one tone with the frequency $f = f_1 + \frac{\Delta f}{2}$, amplitude modulated with Δf. If the difference between the two tones exceeds approximately 15 Hz, a roughness or discomforting sound occurs. When Δ_f is increased furthermore, two single tones are perceived, corresponding to frequencies f_1 and f_2. [MJ18] The caused local resonances on the basilar membrane are spread far enough to hear two different pitched signals, but the sound is still perceived rough. Suppose the frequency difference gets larger than the critical bandwidth (f_{CB} or bark-bands) of the inner ear, the roughness decreases, and both tones sound smooth and pleasant. Separating the two tones with a headphone also resolves the perceived roughness, showing the physical limitations on frequency resolution of the inner ear. A comprehensive overview of different roughness models is shown in [Son98].

Although roughness is not the main characteristic of air noise in microspeaker systems, it can be an indicator for identifying different failure modes occurring over the sweep excitation. Plots for the residual and original signal are shown in the appendix in figure D.10 and D.11.

Sharpness

Like loudness, sharpness is a comparative measure, in the unit accum. It is essential for assessing the timbre of a sound and is an indicator of the spectral balance between low and high frequencies. [Bis74] The higher the frequency contents of a signal, the sharper it is perceived. For low-level signals (below 90 dB(SPL)), the amplitude dependency of sharpness can be neglected. [ZF13] The spectral envelope of noise is the fundamental characteristic of sharpness perception. It is calculated with a weighted integral over the bark scales specific loudness levels, normalised by the total

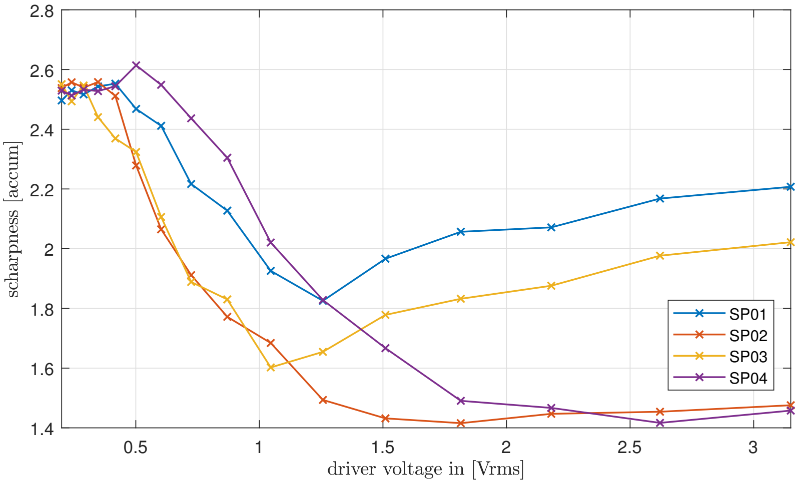

Figure 3.20.: Sharpness of the residual over increasing driver voltage at the 1/3-octave band around 100Hz

loudness level and a reference sound. As a comparative measure, the ratio of different sounds can be perceived half as sharp, five times as sharp, etc. The reference sound for "one accum" sharpness is a 1 kHz narrowband noise at 60 dB(SPL) and bandwidth of $\Delta f = 160$ Hz, corresponding to the critical band. The bandwidth of a sound is a crucial variable affecting sharpness. If a low-frequency sound is added to an existing sound, it can reduce the original sharpness, resulting in a louder but "less annoying" or "less disturbing" sound. [Son98] [ZF13]

In figure 3.20 the sharpness of the residual shows bad SNR at low driver voltages, and for higher voltages, it clearly shows a less noisy performance for SP02 and SP04. SP03 reveals the most sharpness in the residual evaluated over the total frequency range shown in the appendix in figure D.13. Figure D.12 presents the sharpness of the original signal over the whole frequency range. Higher THD at the exponential ports (SP02/SP04) seem to increase sharpness.

4. Parameter correlations and clustering

The non-harmonic distortion parameter (NHD) is a good indicator for the evolution of port noise, but rating the port's performance still is difficult, especially if multiple failure modes exist. The correlation to the Reynolds number at 100 Hz underpins the detection of the onset of air noise in the NHD parameter. Still, following this assumption, air noise is detectable at relatively low amplitudes for most investigated ports, although it might not be audible.

In section 3.5 three objective parameters (THD, NHD and SPL) were introduced and five psychoacoustic parameters (dB(A), N, LN, SCH, R) are introduced in section 3.6, yielding a set of eight parameters. The psychoacoustic parameters are calculated once for the residual and once for the original signal. THD and SPL are solely calculated for the original signal, and calculations for the NHD are only defined for the residual. All parameters are calculated for six representative frequency supporting points at [100, 200, 400, 600, 800, 900 Hz], resulting in a $13 \times 6 = 78$ size parameter set for each sound port over 16 driver voltage levels.

First, a principal component analysis (PCA) is used to classify port noise exclusively on the parameters calculated from the residual (NHD, dB(A), N, LN, SCH and R), shown in figure 4.3. Clustering the ports at the 1/3-octave band around the 100 Hz frequency supporting point is possible (at 100 Hz the velocity is nearly the same for all ports). An additional listening test confirms the analytic approach at 100 Hz (section 4.2). Still, a distinct separation of air noise from other distortions and failure modes is impossible over the total frequency range. Failure modes change too much during the sweep's excitation time. Therefore, a second parameter set (THD,

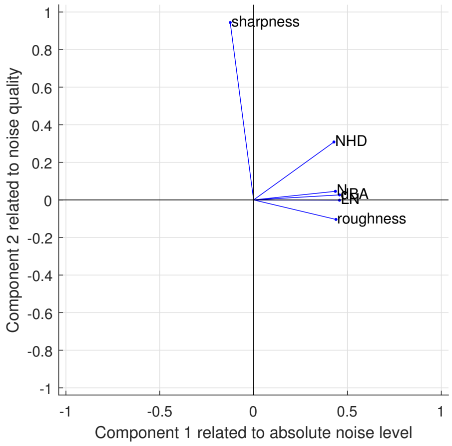

Figure 4.1.: Loading plot of the first parameter set (NHD, dB(A), N, LN, SCH and R) calculated only from the residual for all 4 ports, 6 representative frequency supporting points and 16 driver voltages

NHD, L, L_{res}, R, Sch_{res}) is selected for a PCA with combined parameters calculated from the original and the residual signal yielding a suitable 2D representation or "fingerprint" for a more generic port performances evaluation (figure 4.5). The sub index $_{res}$ in the second parameter set now indicates parameters calculated from the residual signal.

4.1. Principle component analysis

A principal component analysis is used to project high dimensional correlated data to the orthogonal eigenbasis of the covariance matrix, resulting in low dimensional uncorrelated data with minimum information loss. Before using the PCA, the selected parameter set is standardised by calculating the z-scores. The z-score implementation of MATLAB is used in the present work. The implementation is defined as,

$$z = \frac{x - \mu}{\sigma} \tag{4.1}$$

with x being a calculated parameter value, μ the mean and σ the standard deviation of the total data vector for each parameter, respectively. "The

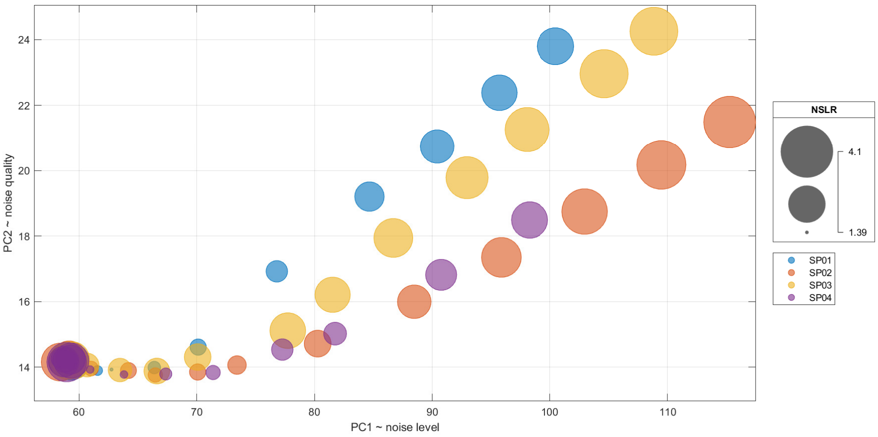

Figure 4.2.: Sound port cluster with PCA. The used parameters are calculated only from the residual signal shown for the frequency supporting point at 100 Hz. The bubble size is proportional to the noise to signal loudness ratio (NSLR)

standardised data set has zero mean and standard deviation 1, and retains the shape properties of the original data set (same skewness and kurtosis). " [MAT22b]

Parameter set for port noise evaluation

The loading plot in figure 4.1 shows how much each parameter contributes to the first two principal components (PC). In other words, it shows the loadings for the parameters on the orthogonal eigenvectors of the two largest eigenvalues of the covariance matrix. The angles between parameters indicate how correlated they are. It is shown that, e.g., different loudness measures are highly correlated with each other, and sharpness is nearly uncorrelated with the other parameters. The loadings for the first two principal components also reveal a rudimental interpretation of the high dimensional parameter set. The first principal component relates to the absolute noise level, and the second PC gives information about the noise quality in the residual. The total covered variance is 94% of the high dimensional data for the first parameter set. Projecting the parameters calculated from the residual signal on the first two principal components shows clustering for the four ports. The bubble plot in figure 4.2 shows the four sound ports for all driver voltages at the frequency supporting point of 100 Hz. Bubbles is the lower left corner correspond to low driver voltages and bubbles in the upper right corner correspond to the highest driver voltages (3.15 Vrms). The bubble size indicates the noise to signal loudness ratio (NSLR) introduced in equation 3.13. Data points in the lower-left corner indicate low noise level and low noise quality (no air noise). Data points in the upper

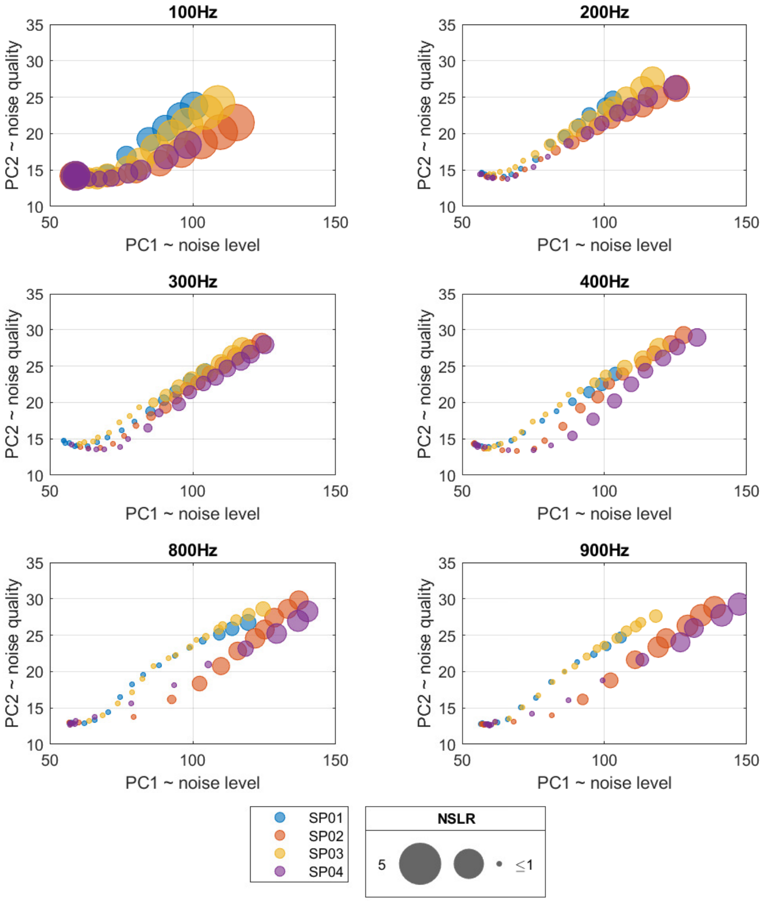

Figure 4.3.: Sound port cluster with PCA, used parameters are calculated only from the residual signal shown for representative frequency supporting point

right corner indicate high noise levels and more noise quality, e.g. sharper sounds. The face colour of the bubbles corresponds to different ports.

In figure 4.2 SP04 outperforms the other three ports even at the highest voltage (3.15 Vrms). Other ports reach similar noise performance only if the voltage is reduced to approximately 2 Vrms. It is also shown that the sound ports without radii (SP01/SP03) produce sharper noise than the others and SP02 has the worst NSLR. Larger sized data points at low levels (lower left corner) show bad SNR. At low levels the spread of the data points is lower than the size of the high SNR bubbles, but all ports show consecutive data points with increasing driver voltage, correlated to air noise.

A noise performance representation of the ports is shown in figure 4.3 over all selected frequency supporting points. Rating the ports definite good or bad, is not possible because their performance changes too much over the sweep excitation time (with velocity). The NSLR is the highest at 100 Hz, and therefore, the performance evaluation at this frequency is the most significant, but sound ports SP02 and SP04 also show high NSLR at high frequencies, which might be problematic.

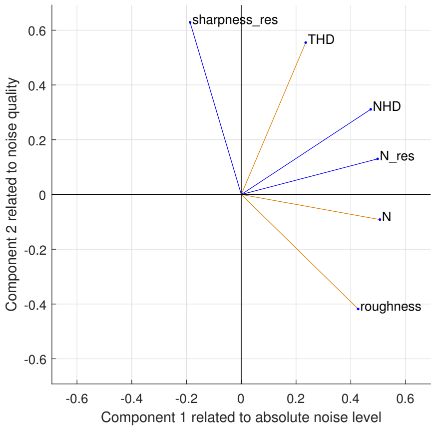

Figure 4.4.: Loading plot of the 2nd parameter set (THD, NHD, N, N_{res}, R, Sch_{res}) parameters calculated from both the original signal (in orange) and residual signal (in blue) for all 4 ports, 6 representative frequency supporting points and 16 driver voltages

Parameter set for general port performance

The second parameter set (THD, NHD, N, N_{res}, R, Sch_{res}) represents the generic behaviour of sound ports, not only concerning its noise. Figure 4.4 shows the loadings for the 2nd parameter set, with a covered variance of 80%. The first PC correlates to the absolute loudness, and the second axis (PC2) shows the noise quality representing information about the sharpness of the residuum and the THD. The roughness contributes the same amount to each principal component but points in the negative direction of PC2. Suppose the trajectory of a port over increasing voltage moves in the negative direction on the y-axis (PC2). In that case, this indicates a rising roughness (e.g. SP04 lower right plot in figure 4.5 at 800 and 900 Hz).

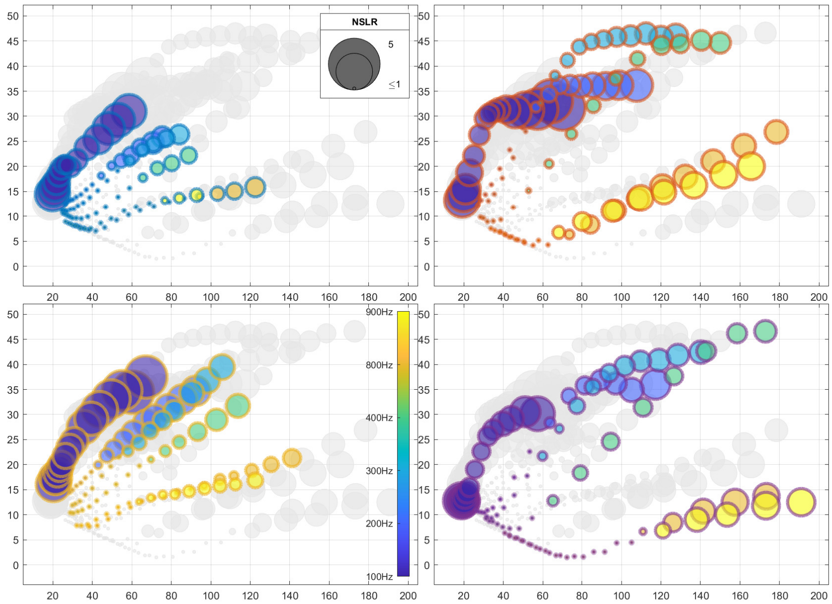

Figure 4.5.: Sound port cluster over significant frequency steps with 2nd parameter set (upper left SP01, upper right SP02, lower left SP03, lower right SP04)

An overview of the general port performance serving as "fingerprint" of a port is shown in figure 4.5. The edge colour indicates the sound ports, and the face colour of the bubbles indicates the frequency matching the shown colour bar. The velocity dependency is visible on the first look - bubbles over corresponding frequency trajectories show different behaviours. SP01 and SP03 show a more linear and constant behaviour over different driver levels and frequency supporting points, corresponding to their simpler straight and flared shape. The exponentially shaped ports (SP02/04) play louder while producing moderate NSLR except for high frequencies. SP02 and SP04 show high THD levels at 300 and 400 Hz, and all ports have relatively high NSLR at 100 Hz.

4.2. Additional listening test

A listening test was performed in the company Sound Solutions (SSI) by Stefan Kaiser to validate findings from the analytic solution presented in the present work. A small amount of seven subjects were asked to rate sound port recordings on a scale from $0 =$ strongly dislike to $10 =$ strongly like. The recording set consisted of one second long, 100 Hz static sine tones recorded for the four sound ports at the near-field microphone position, each for the highest five voltage steps normalised to common gain. Playback was done on a *Beyerdynamic DT-770* headphone, and the subjects were able to listen to all 20 files multiple times. An interface was offered with randomised order of the recordings and a play button next to them. Subjects were asked to rate each file by preference using sliders in the same interface.

Figure 4.6 shows the standardised port ratings from the listening test over the seven subjects. Each subject's results were centred on the individual mean (marked with a circle in figure 4.6) and scaled with the corresponding standard deviation. The delta ratings use SP01 at 1.05 Vrms as a reference. On the y-axis, the cumbersomeness of the ports is shown from 0 to 10, with 10 being the worst. Port ratings confirm the dependency of noise to the amplitude, meaning that higher voltage levels introduce more noise or "disliking" of the sound. The 95% confidence intervals (marked with bars) are relatively large because of the small number of test persons and the different time spent on the test between subjects. At 100 Hz, SP02 and SP03

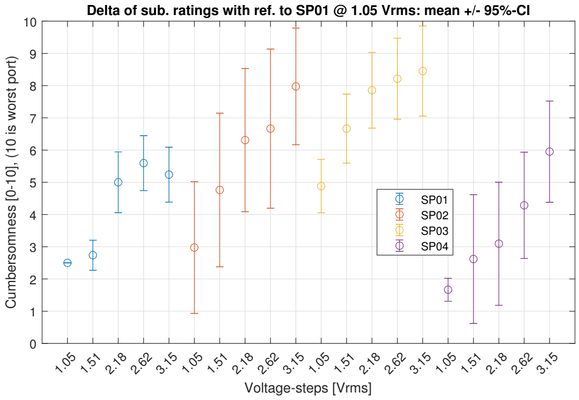

Figure 4.6.: Listening test ratings for a static 100Hz sine tone over the 5 highest voltage steps (1 to 3Vrms)

have the highest cumbersomeness indicating higher audible noise than the straight SP01 and SP04 with the largest diameter.

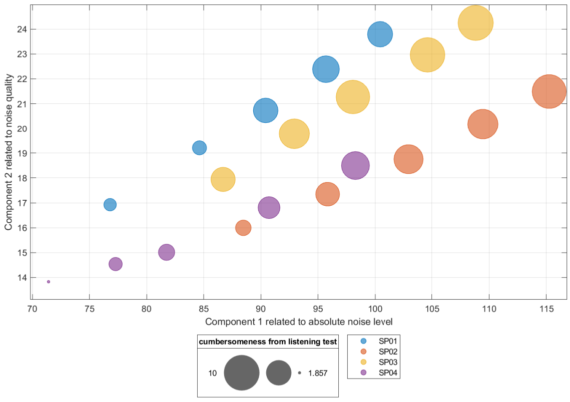

Figure 4.7.: Sound port cluster with PCA, data set shown for 100Hz, rated with cumbersomeness from listening tests

Rating the data in figure 4.2 with the mean value of the listening tests' cumbersomeness shows similar results to the rating with the NSLR, again indicating validity for the chosen approach on port noise investigations.

4.3. Conclusion and outlook

The Reynolds number confirms the possibility of detecting the onset of air noise with the presented NHD parameter. Clustering sound ports with a PCA yields a fingerprint for port identification. However, a generic solution would need a much larger data set to classify different sound port geometries. Psychoacoustic parameters provide deeper insight into the perceptual level and quality of noise. The shown approach is a reliable method to compare sound ports on their produced port noise, but an absolute level for the audibility of noise is missing. Further investigations towards air noise audibility in real-world applications is necessary. The theory found in the literature on bass-reflex speakers is confirmed for micro-speaker systems. The most significant differences to the literature rise from the much smaller dimensionality, resulting in higher port resonances. The author plans to use this analysis method to measure more ports with only slightly changing port geometries, yielding a state-space parameter model that provides more insight into the geometrical design process for an optimal port.

Appendix

Appendix A.

Driver speaker specifications

Driver Specification Sheet

Model No:: PLS-P830970
Product Line: Peerless

Rev: 1
Last Update: 2017-04-25 21:32:09

Product Description

This 2 inch 4 ohm member of the PLS family sets a high standard for compact full range drivers intended for applications such as television soundbars and compact music systems. Design features in this family include a damped plastic basket with venting under the spider to aid cooling of the motor, a neodymium magnet motor with copper cap to lower coil inductance, providing low distortion at low frequencies and extended high frequency response. A black anodized aluminium cone is employed on the driver, along with a black anodized aluminium dust cap coupled directly to the voice coil. Additionally, the cones come equipped with special-designed large roll rubber surrounds, which allow for a dynamic linear response to high excursion input signals.

Mechanical Drawing

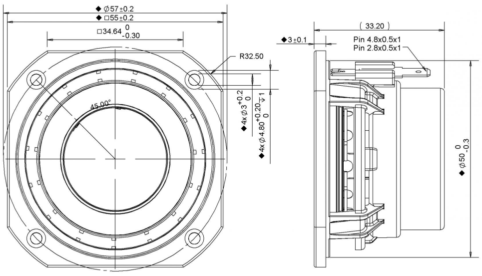

Specifications

DC Resistance	Revc	Ohms	3.6	5.0%	Energy Bandwidth Product	EBP	(1/Qes)*fs	
Minimum Impedance	Zmin	Ohms	4.02	7.5%	Moving Mass	Mms	g	1.4
Voice Coil Inductance	Le	mH	0.03		Suspension Compliance	Cms	um/N	661.1
Resonant Frequency	Fs	Hz	165.78	15%	Effective Cone diameter	D	cm	4.2
Mechanical Q Factor	Qms		3.85		Effective Piston Area	Sd	cm^2	13.9
Electrical Q Factor	Qes	0.67			Effective Volume	Vas	L	0.18
Total Q Factor	Qts		0.57		Motor Force Factor	BL	Tm	2.79
Ratio Fs/Qts	F	Fs/Qts	289.82		Motor Efficiency Factor	ß	(T*M^2)/Ohms	2.2
Half Space Sensitivity @2.83V	db@2.83V/1M	dB	85.29	+/- 1.0db	Voice coil former Material	VCfm		ASV
Half Space Sensitivity @1W/1M	db@1W/1M	dB	82.3	+/- 1.0db	Voice coil inner diameter	VCd	mm	25.73
Gap Height	Gh	mm	3		Rated Noise Power	P	W	25
Maximum Linear Excursion	Xmax	mm	1.7		Test Spectrum Bandwidth	150Hz - 20kHz		
Ferrofluid Type	FF				Driver Size	Inch	2 in	
Driver Mass	Kg	0.14						

Frequency and Impedance Response

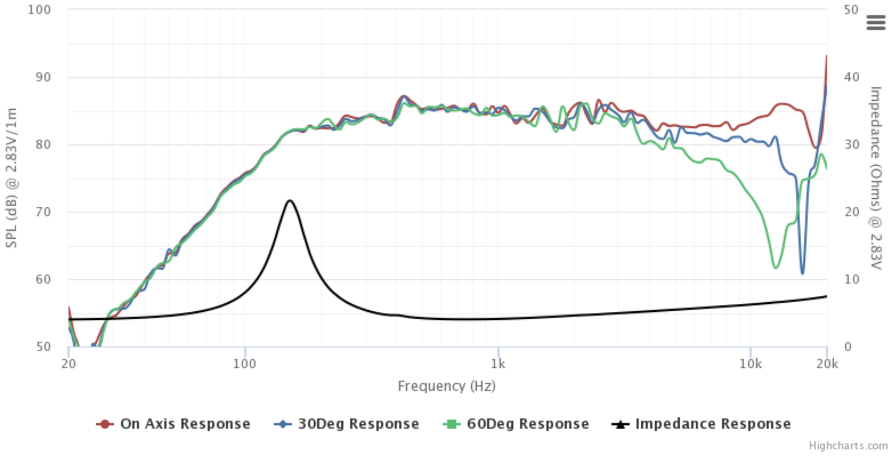

Appendix B.

All ports: angle dependent high-frequency damping and air jet stream effect

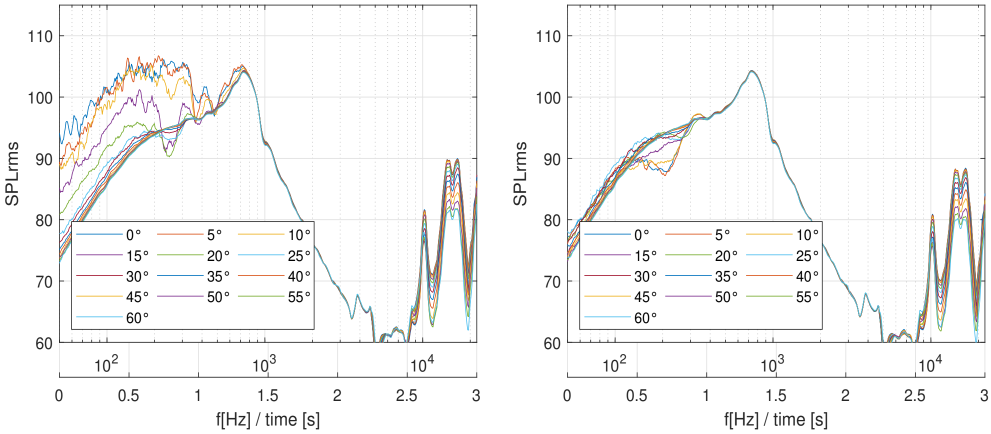

(a) Port 1

(b) Port 1 with windshield

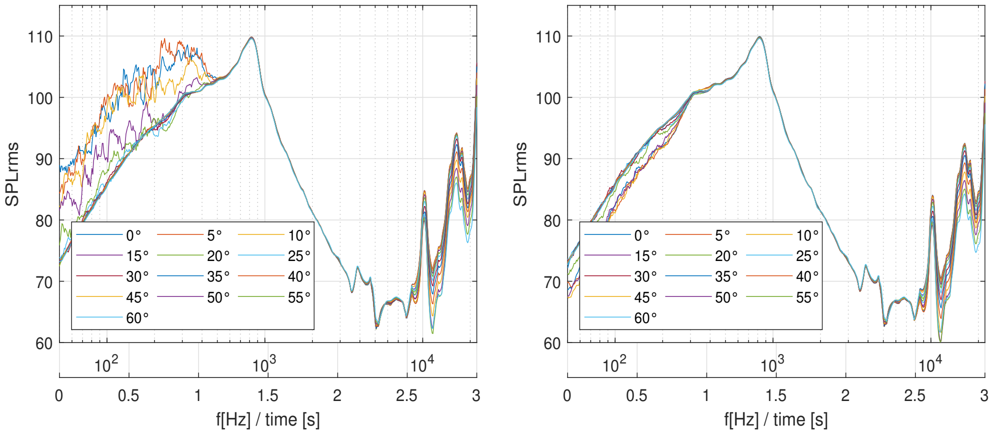

(c) Port 2

(d) Port 2 with windshield

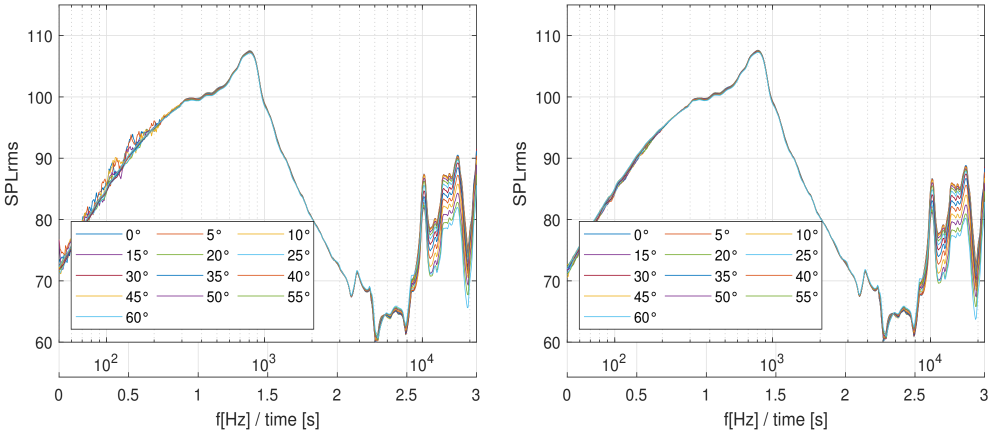

(e) Port 3 (f) Port 3 with windshield

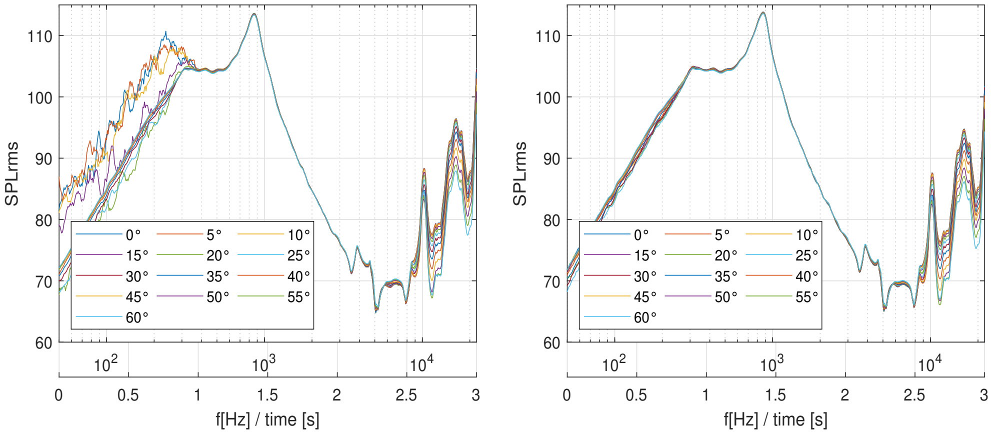

(g) Port 4 (h) Port 4 with windshield

Figure B.1.: Angle dependency and air jet stream over angle for all ports

Appendix C.

Airjet stream measurement distortions

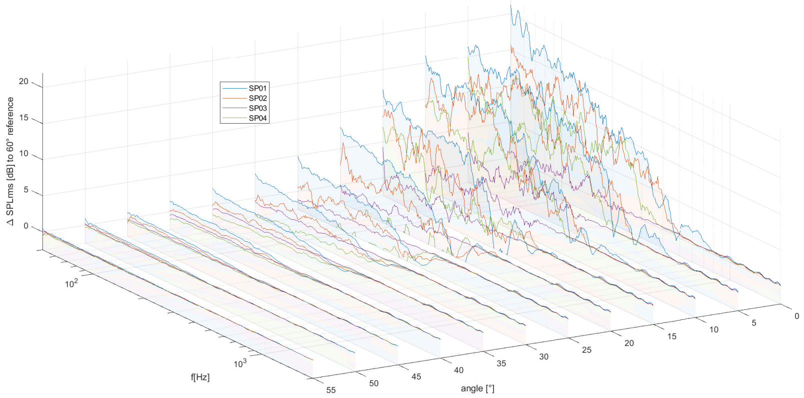

(a) All ports without windshield

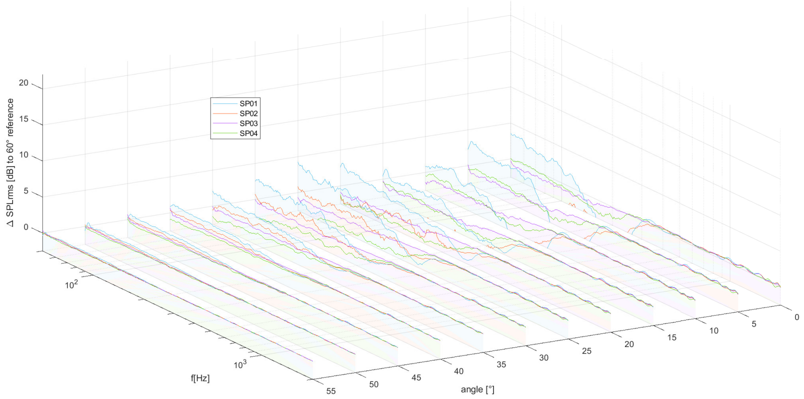

(b) All ports with windshield

Figure C.1.: Airjet stream measurement distortions appearance over angle for all ports

Appendix D.

Acoustic and psychoacoustic parameters

Sound pressure level (SPL)

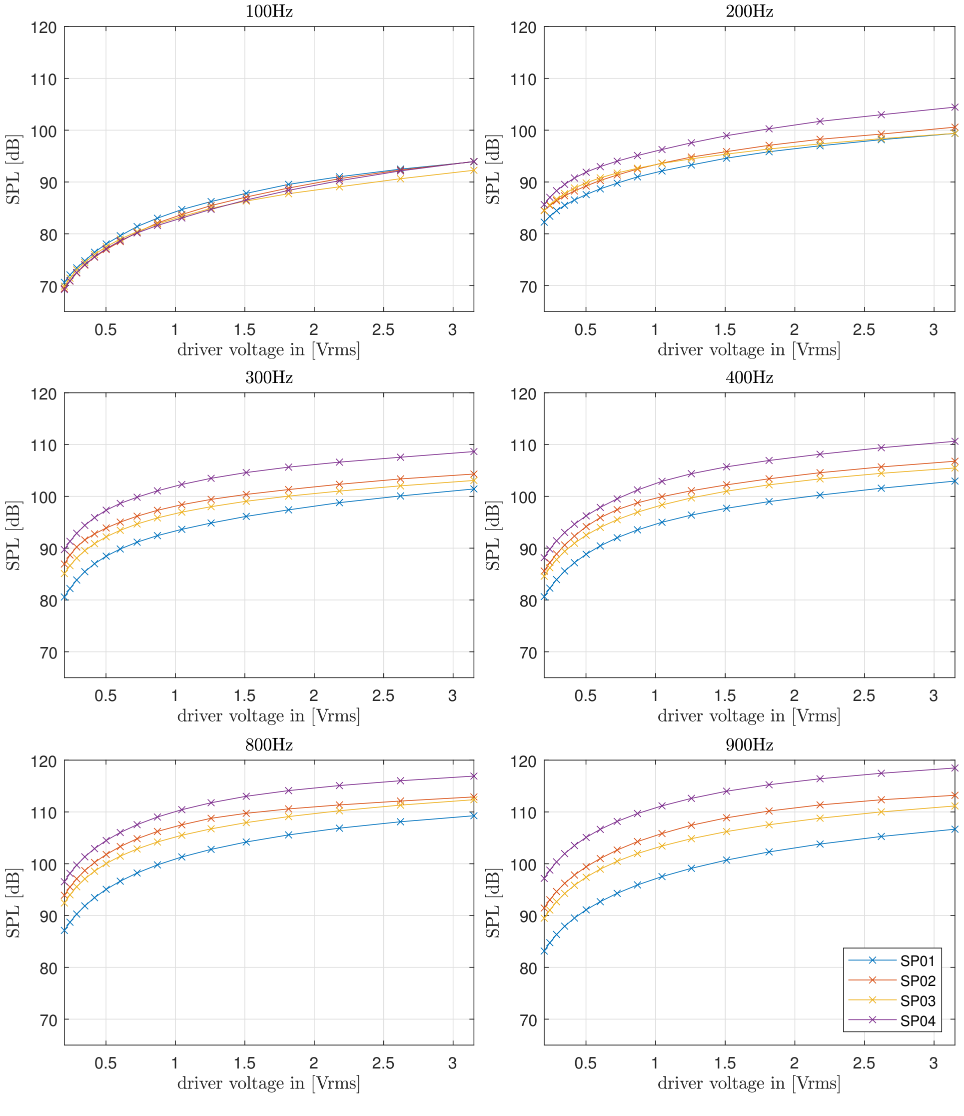

Figure D.1.: Sound pressure level (SPL) over driver voltage for representative frequency support points

Total harmonic distortion (THD)

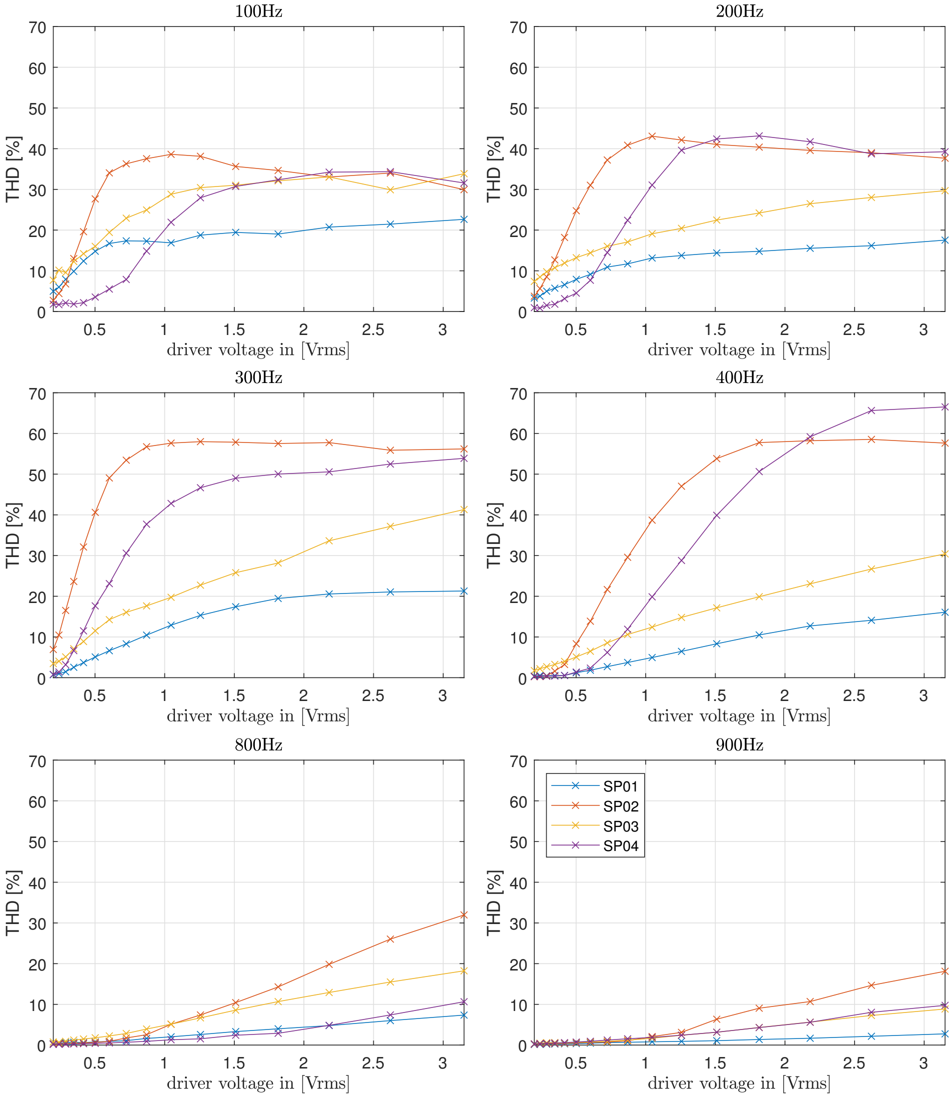

Figure D.2.: Total harmonic distortion (THD) over driver voltage for representative frequency support points

Non-harmonic distortion (NHD)

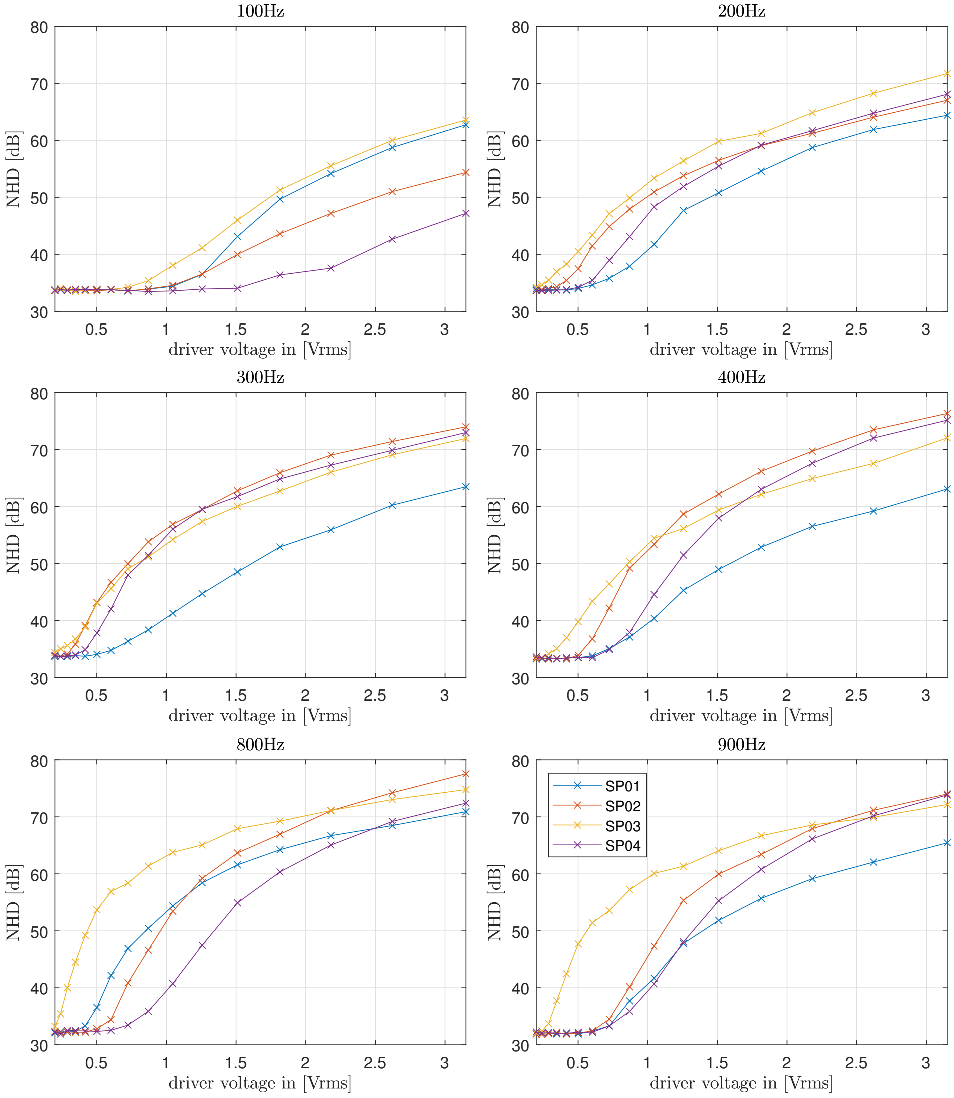

Figure D.3.: Non-harmonic distortion (NHD) over driver voltage for representative frequency support points

Normalised non-harmonic distortion (nNHD)

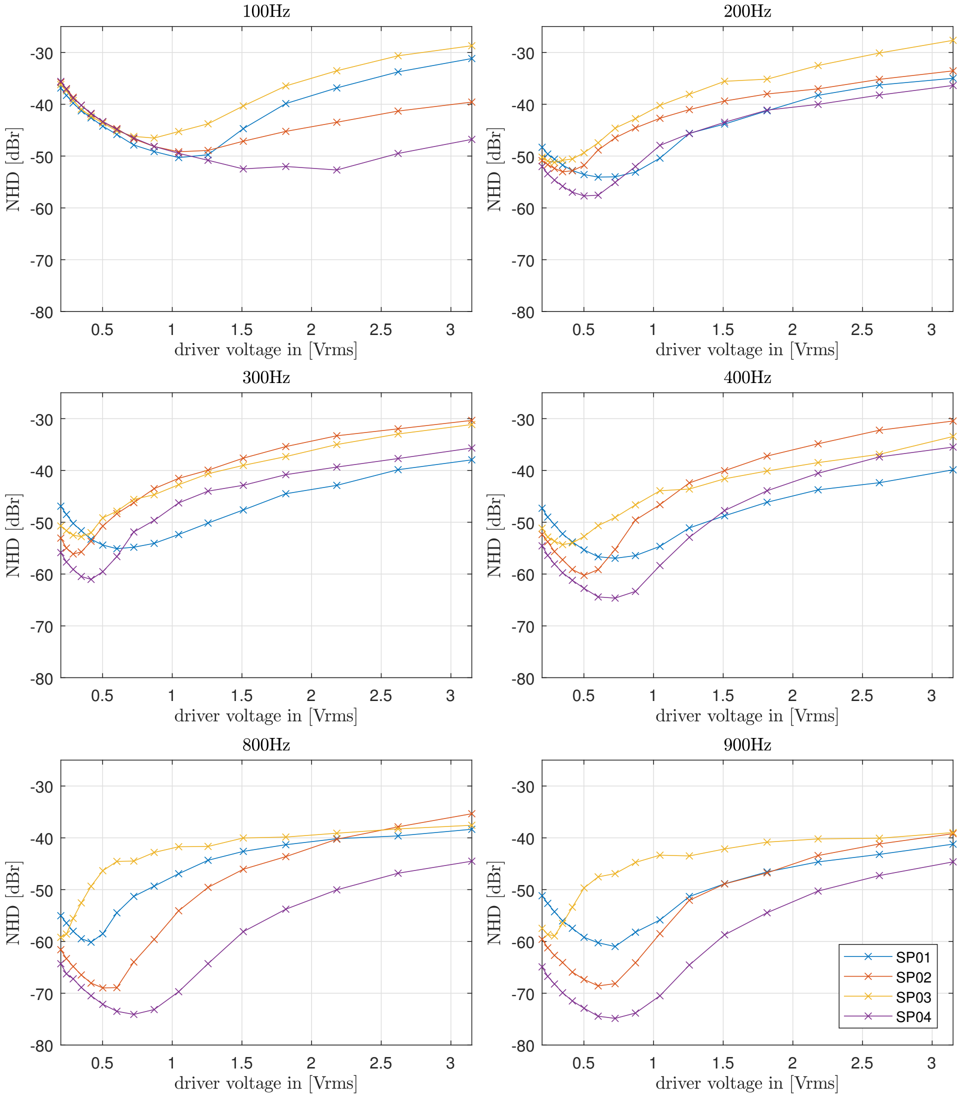

Figure D.4.: Normalised non-harmonic distortion (nNHD) over driver voltage for representative frequency support points

Loudness level, original signal

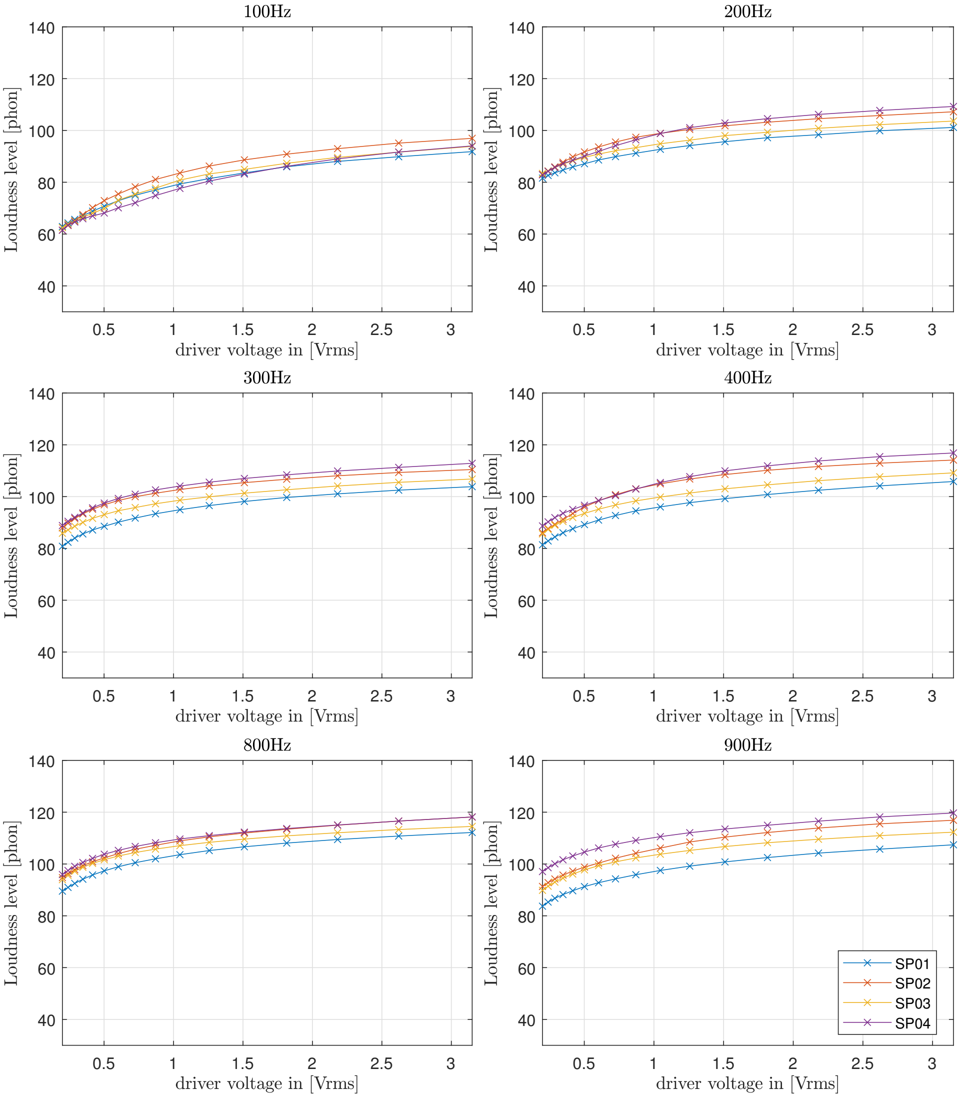

Figure D.5.: Loudness level by Zwicker over driver voltage for representative frequency support points, original signal

Loudness level, residual

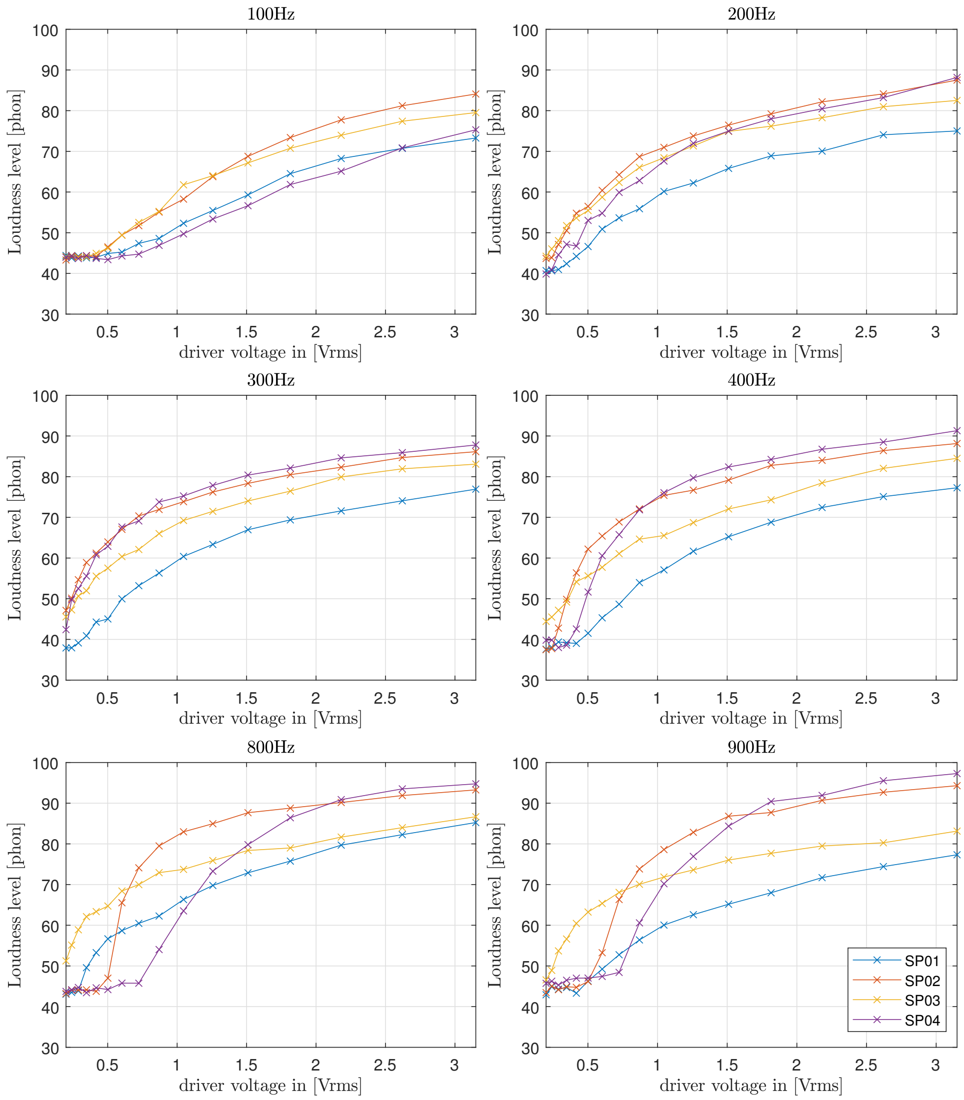

Figure D.6.: Loudness level by Zwicker over driver voltage for representative frequency support points, residual

Loudness, original signal

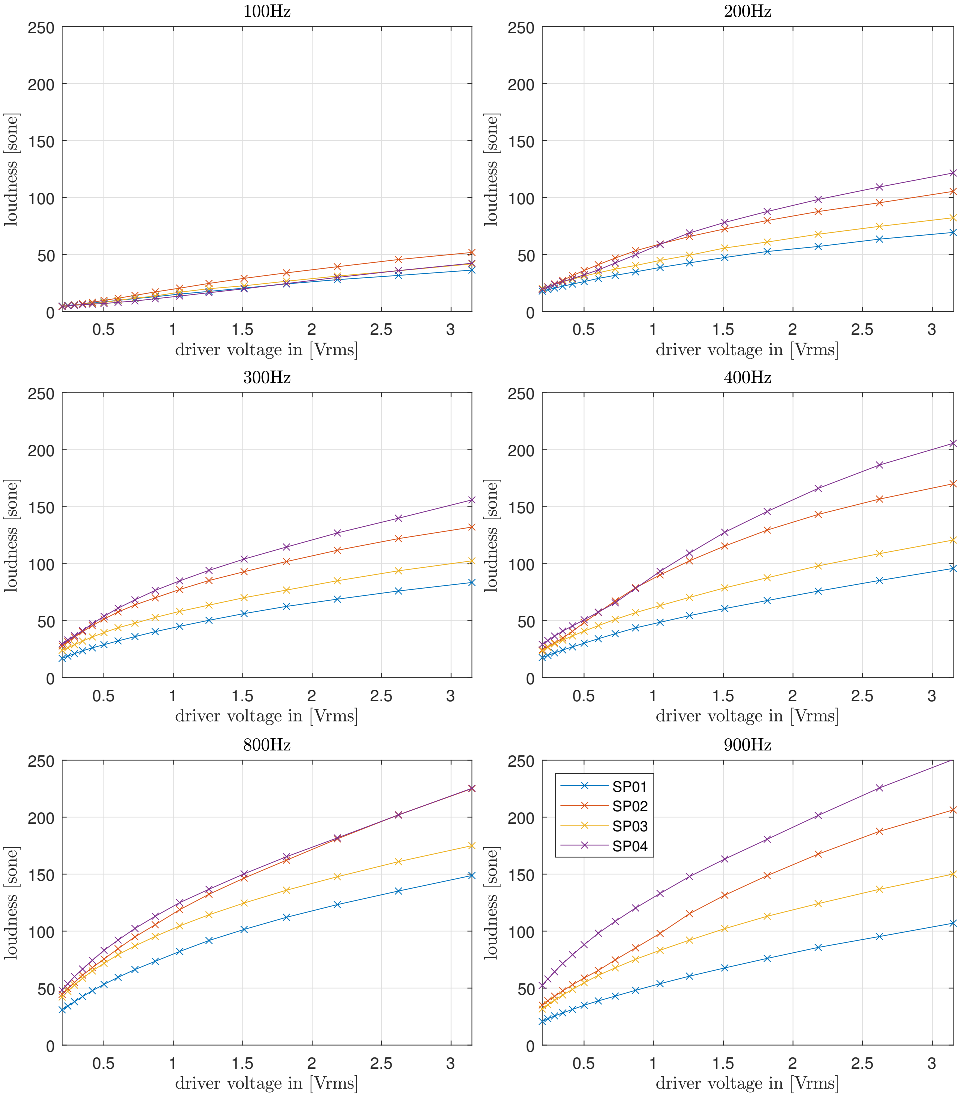

Figure D.7.: Loudness by Zwicker over driver voltage for representative frequency support points, original signal

Loudness, residual

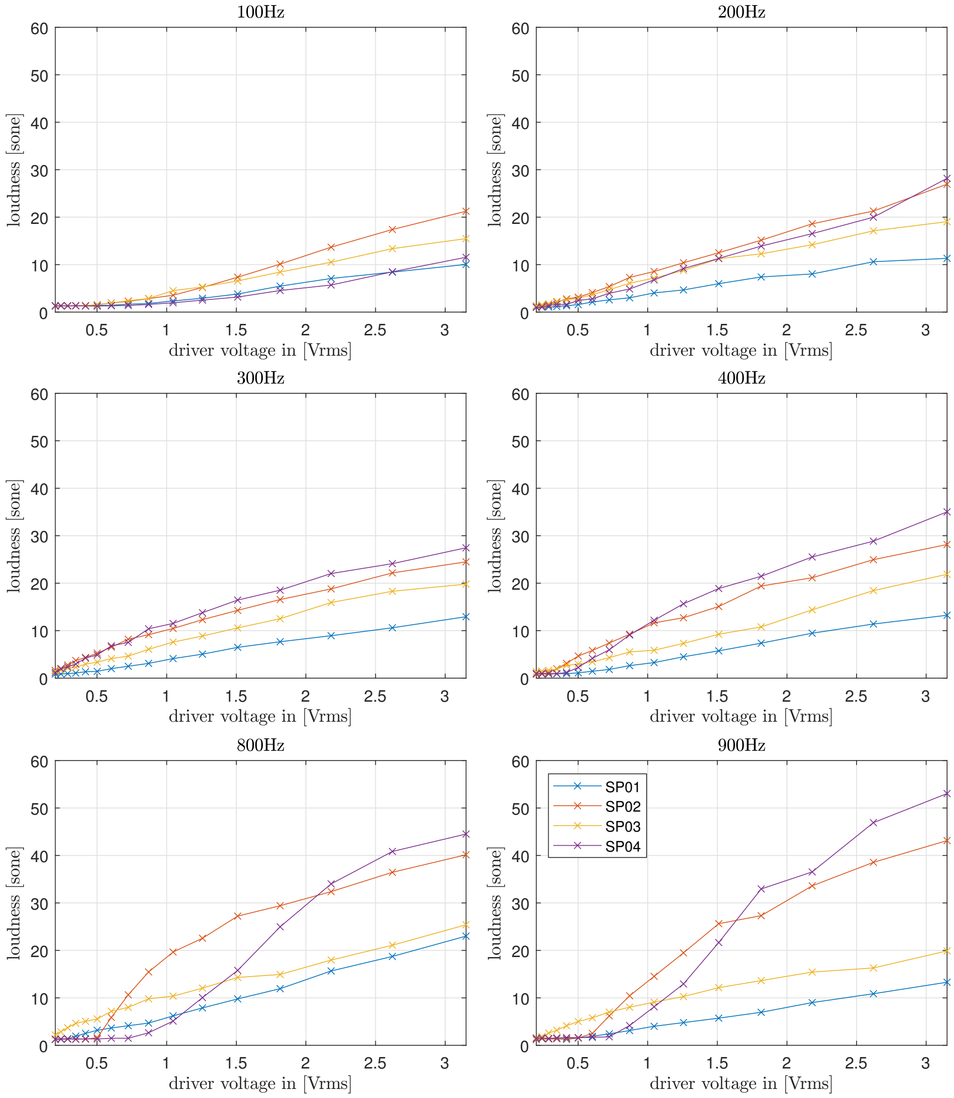

Figure D.8.: Loudness by Zwicker over driver voltage for representative frequency support points, residual

Noise to signal loudness ratio (NSLR)

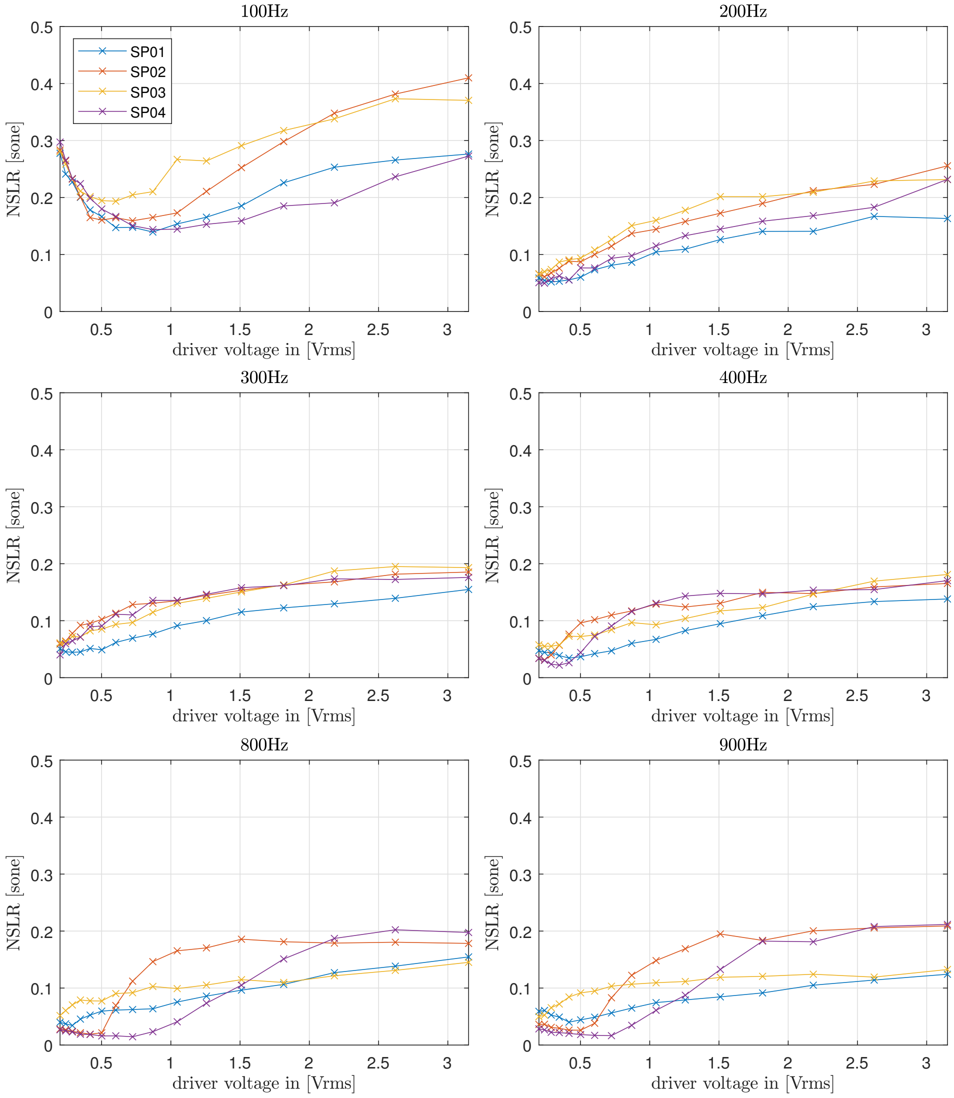

Figure D.9.: Noise to signal loudness ratio (NSLR) over driver voltage for representative frequency support points

Roughness, original signal

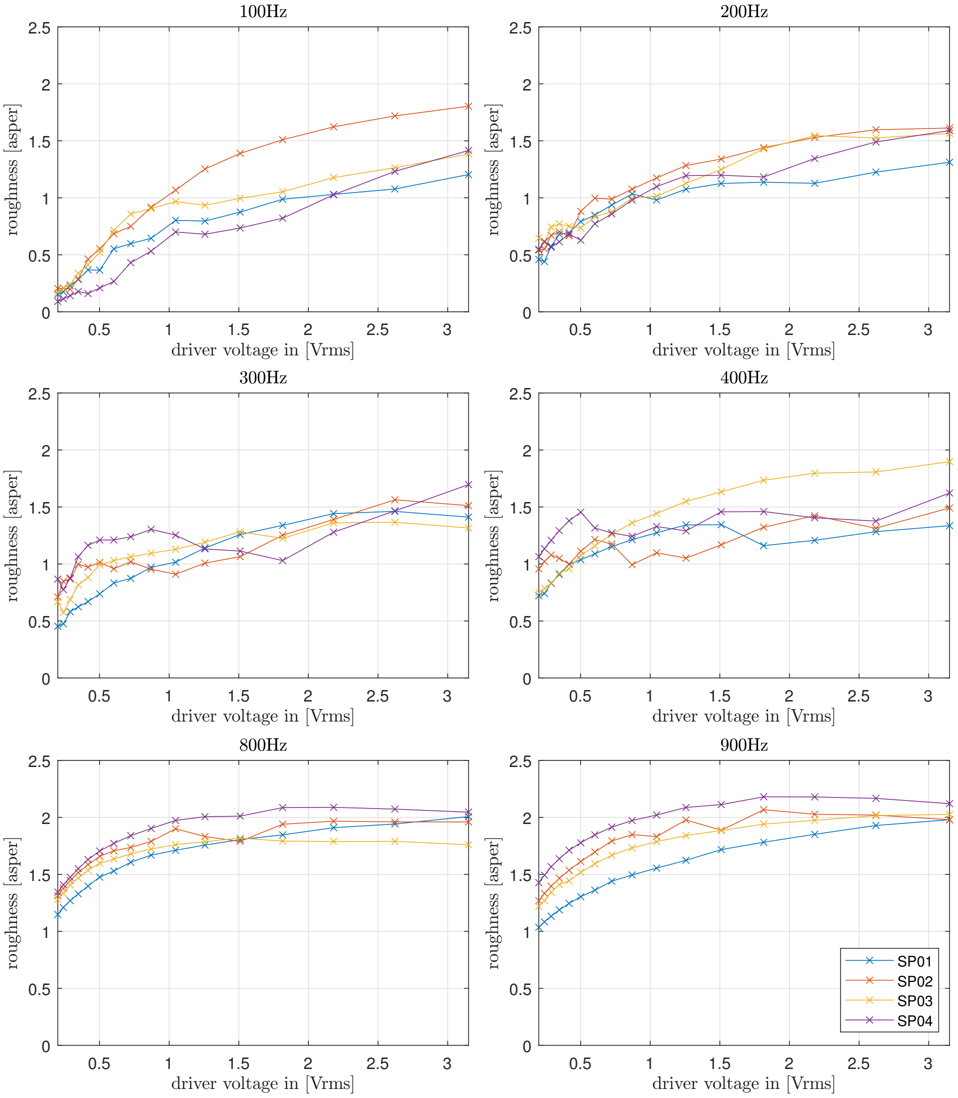

Figure D.10.: Roughness over driver voltage for representative frequency support points, original signal

Roughness, residual

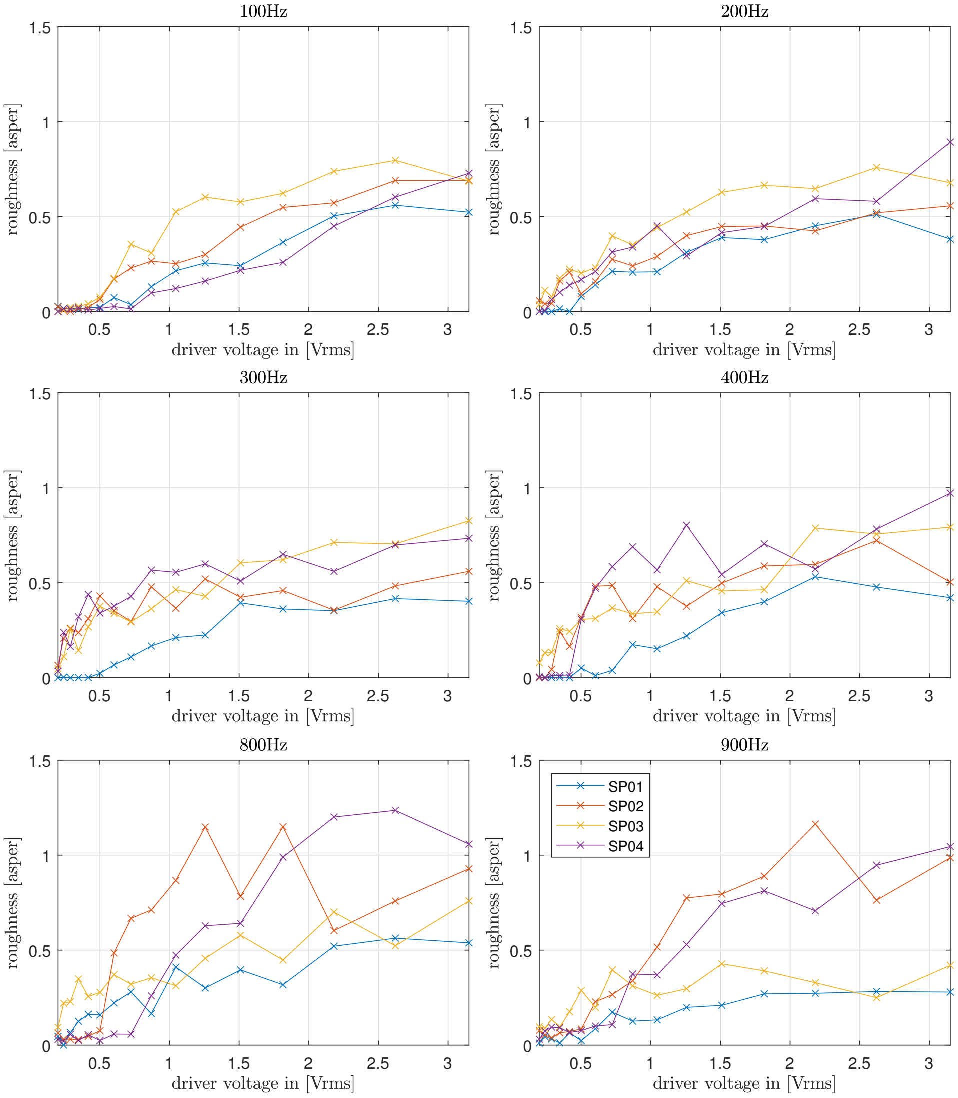

Figure D.11.: Roughness over driver voltage for representative frequency support points, residual

Sharpness, original signal

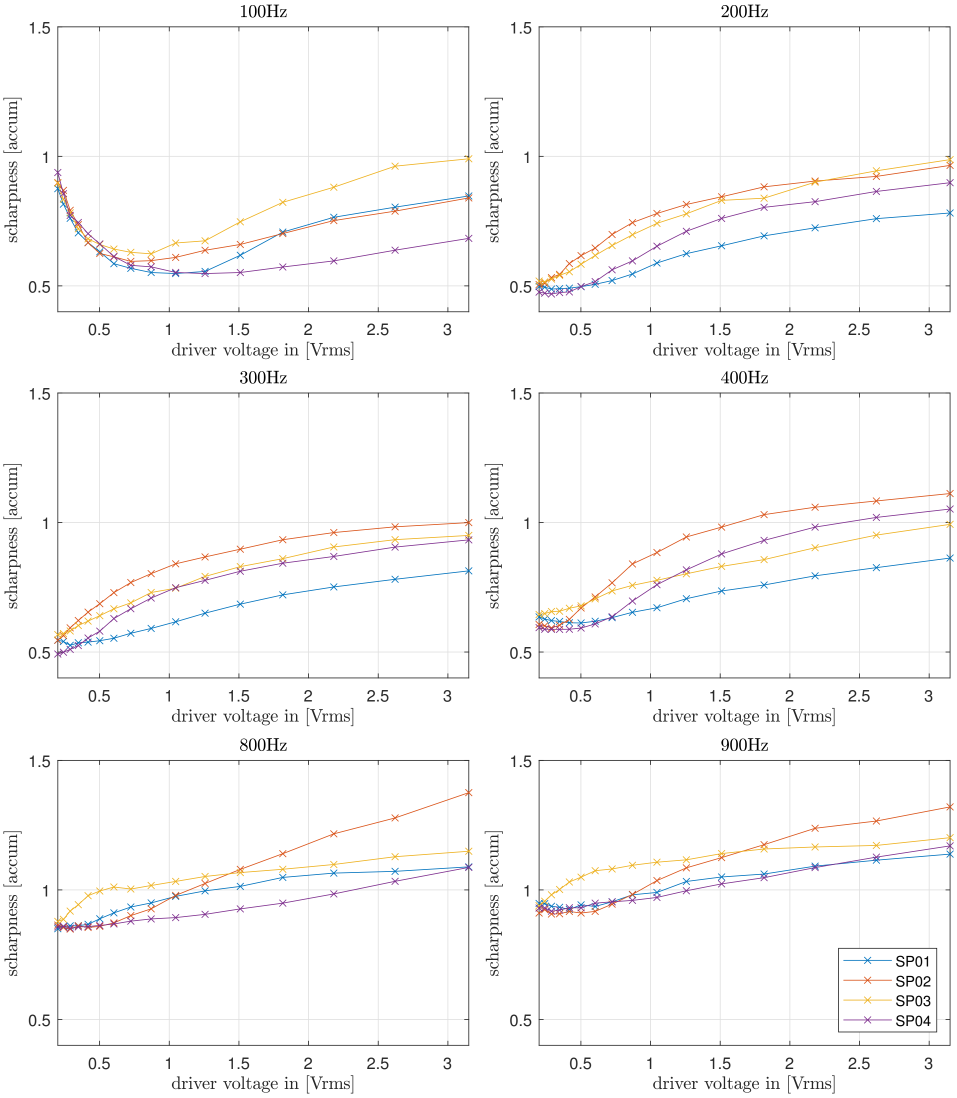

Figure D.12.: Sharpness over driver voltage for representative frequency support points, original signal

Sharpness, residual

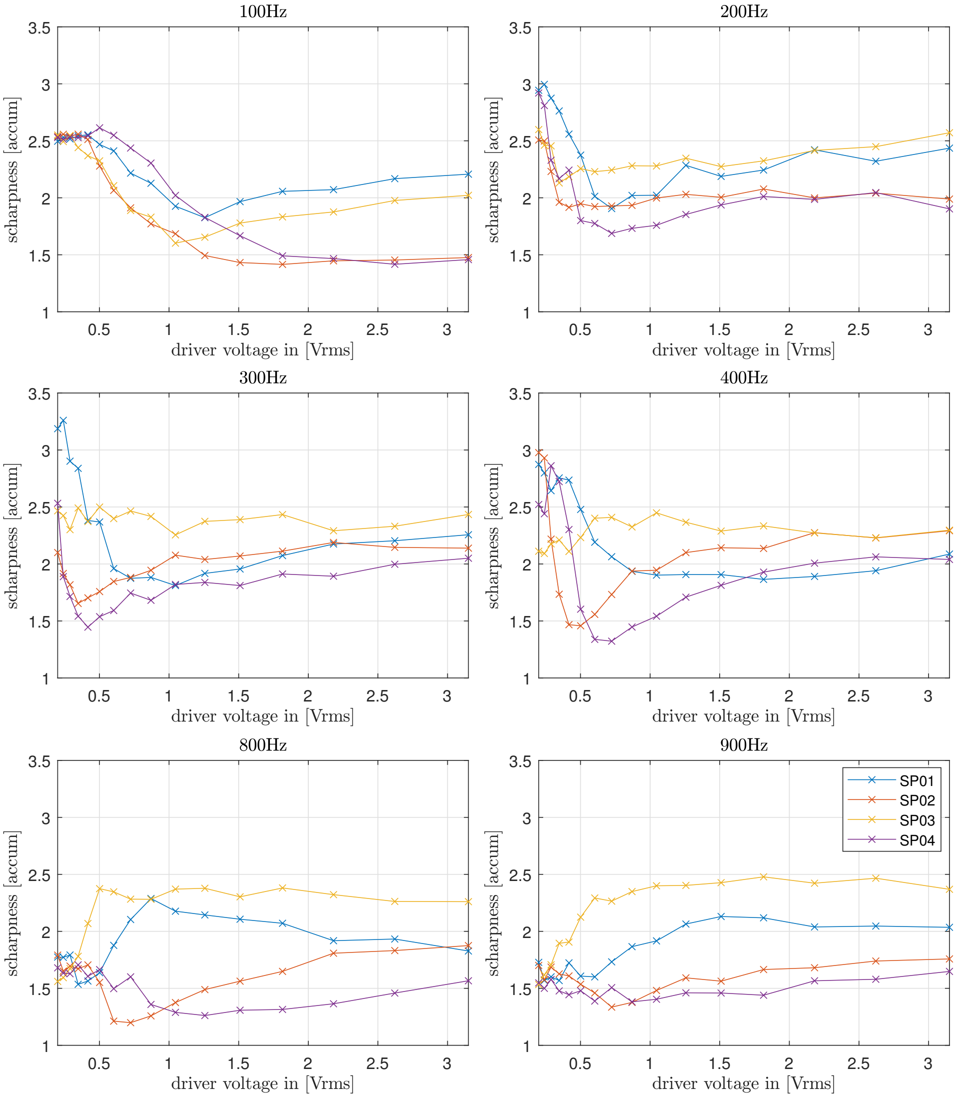

Figure D.13.: Sharpness over driver voltage for representative frequency support points, residual

Bibliography

[And20] Allan O. Devantier Andri Bezzola, Glenn S. Kubota. "Acoustic Mass and Resistance as Function of Drive Level for Straight, Bent, and Flared Loudspeaker Ports." In: *149th Audio Engineering Society International Convention, AES 2020* (2020) (cit. on p. 8).

[Aur85] Wilhelm Aures. "Ein berechnungsverfahren der rauhigkeit." In: *Acta Acustica united with Acustica* 58.5 (1985), pp. 268–281 (cit. on p. 54).

[Bac16] Juha Backman. "Fluid dynamics analysis of ported loudspeakers." In: *141st Engineering Society International Convention 2016* 1 (2016), pp. 2–7 (cit. on p. 6).

[Bac17] Juha Backman. "Nonlinearity of ported louspeaker enclosures." In: *142nd Audio Engineering Society International Convention 2017, AES 2017* (2017), pp. 1–7 (cit. on p. 7).

[Bac95] Juha Backman. "The nonlinear behavior of reflex ports." In: *Audio Engineering Society Convention 98* 3999 (1995) (cit. on pp. 5, 17).

[BDM19] Andri Bezzola, Allan Devantier, and Elisabeth McMullin. "Loudspeaker port design for optimal performance and listening experience." In: *147th Audio Engineering Society International Convention 2019* (2019) (cit. on pp. 4, 5, 7).

[Bez19] A Bezzola. "Optimal Bass Reflex Loudspeaker Port Design." In: (2019) (cit. on pp. 3, 13, 14).

[Bis74] Gottfried von Bismarck. "Sharpness as an attribute of the timbre of steady sounds." In: *Acta Acustica united with Acustica* 30.3 (1974), pp. 159–172 (cit. on p. 55).

[Bri06] Eddy B. Brixen. "Wind generated noise in microphones - An overview - Part II." In: *Audio Engineering Society - 121st Convention Papers 2006* 1 (2006), pp. 230–237 (cit. on pp. 24, 27).

[Bru+17] P. Brunet et al. "Use of Repetitive Multi-Tone Sequences to Estimate Nonlinear Response of a Loudspeaker to Music." In: *Journal of The Audio Engineering Society* (2017) (cit. on p. 8).

[But+18] Doug Button et al. "Characterization of nonlinear port parameters in loudspeaker modeling." In: *145th Audio Engineering Society International Convention, AES 2018* November (2018) (cit. on p. 7).

[Far00] Angelo Farina. "Simultaneous Measurement of Impulse Response and Distortion with a Swept-Sine Technique." In: *Journal of The Audio Engineering Society* (2000) (cit. on p. 47).

[FH00] Christian Feldbauer and Robert Höldrich. "Realization of a Vold-Kalman Tracking Filter - A Least Squares Problem." In: *Proceedings of the COST G-6 Conference on Digital Audio Effects (DAFX-00)* 8 (2000), pp. 8–11 (cit. on pp. 31, 33).

[FM33] Harvey Fletcher and W. A. Munson. "Loudness, Its Definition, Measurement and Calculation." In: *The Journal of the Acoustical Society of America* 5.2 (1933), pp. 82–108. DOI: `10.1121/1.1915637`. eprint: `https://doi.org/10.1121/1.1915637`. URL: `https://doi.org/10.1121/1.1915637` (cit. on p. 51).

[Gad+99] S. Gade et al. "Technical review: Characteristics of the Vold-Kalman Order Tracking Filter." In: *Technical Review Brüel&Kjær Sound&Vibration Measurement* (1999) (cit. on p. 32).

[Gar+17] V. M. Garcia-Alcaide et al. "Numerical study of the aerodynamics of sound sources in a bass-reflex port." In: *Engineering Applications of Computational Fluid Mechanics* 11.1 (2017), pp. 210–224. ISSN: 1997003X. DOI: `10.1080/19942060.2016.1277166`. URL: `https://doi.org/10.1080/19942060.2016.1277166` (cit. on p. 7).

[HL95] Vold Havard and Jan Leuridan. “High resolution order tracking at extreme slew rates using kalman tracking filters.” In: *Shock and Vibration* 2.6 (1995), pp. 507–515. ISSN: 10709622. DOI: 10.3233/SAV-1995-2609 (cit. on p. 31).

[How02] M. S. Howe. *Theory of Vortex Sound*. Cambridge Texts in Applied Mathematics. Cambridge University Press, 2002. DOI: 10.1017/CBO9780511755491 (cit. on p. 4).

[II67] Uno Ingard and Hartmut Ising. “Acoustic Nonlinearity of an Orifice.” In: *The Journal of the Acoustical Society of America* 42.1 (1967), pp. 6–17. ISSN: 0001-4966. DOI: 10.1121/1.1910576 (cit. on p. 4).

[Kal15] M. Kaltenbacher. *Numerical Simulation of Mechatronic Sensors and Actuators: Finite Elements for Computational Multiphysics*. Springer Berlin Heidelberg, 2015. ISBN: 9783642401695. URL: http://www.springer.com/de/book/9783642401695 (cit. on p. 4).

[Kun+18] Jan Kunz et al. “Tracking filter design for predictive maintenance of jet engine - Different approaches and their comparison.” In: *Strojnicky Casopis* 68.4 (2018), pp. 75–84. ISSN: 00392472. DOI: 10.2478/scjme-2018-0049 (cit. on p. 33).

[MAT22a] MATLAB. *thd functiion, version 9.11.0.1837725 (R2021b) Update 2*. 2022. URL: https://de.mathworks.com/help/signal/ref/thd.html (cit. on p. 47).

[MAT22b] MATLAB. *Z-score functiion normalize, version 9.11.0.1837725 (R2021b) Update 2*. 2022. URL: https://de.mathworks.com/help/stats/zscore.html (cit. on p. 59).

[MJ18] Christian Maschke and André Jakob. “Psychoakustische Messtechnik.” In: *Psychoakustische Messtechnik*. Ed. by Michael Möser. Berlin, Heidelberg: Springer Berlin Heidelberg, 2018, pp. 1–34. ISBN: 978-3-662-56631-2. DOI: 10.1007/978-3-662-56631-2_1. URL: https://doi.org/10.1007/978-3-662-56631-2_1 (cit. on p. 54).

[RD04] Zachary Rapoport and Allan Devantier. “Analysis and Modeling of the Bi-Directional Fluid Flow in Loudspeaker Ports.” In: *Audio Engineering Society Convention 117* (2004). URL: `http://www.aes.org/tmpFiles/elib/20190520/12851.pdf` (cit. on pp. 4–7, 13, 14).

[RVN98] N Bert Roozen, J E M Vael, and Joris A Nieuwendijk. “Reduction of Bass-Reflex Port Nonlinearities by Optimizing the Port Geometry.” In: *Audio Engineering Society Convention 104* 4661 (1998) (cit. on pp. 5, 15, 17).

[SDB02] Alex Salvatti, Allan Devantier, and Doug J. Button. “Maximizing performance from loudspeaker ports.” In: *AES: Journal of the Audio Engineering Society* 50.1-2 (2002), pp. 19–45. ISSN: 00047554 (cit. on pp. 4, 6, 7, 11, 12, 17).

[Sei21] Maarten van der Seijs. *Second generation Vold-Kalman Order Filtering, MATLAB Central File Exchange*. 2021. URL: `https://www.mathworks.com/matlabcentral/fileexchange/36277-second-generation-vold-kalman-order-filtering` (cit. on p. 31).

[SG16] H Schlichting and K Gersten. *Boundary-Layer Theory*. Springer Berlin Heidelberg, 2016. ISBN: 9783662529195. URL: `https://books.google.at/books?id=bOUyDQAAQBAJ` (cit. on p. 11).

[Son98] Alois Sontacchi. “Entwicklung eines Modulkonzeptes für die psychoakustische Geräuschanalyse unter MatLab.” In: (1998), p. 115. ISSN: 0340-9422 (cit. on pp. 9, 51, 53, 55, 56).

[Tum05] Jiri Tuma. “Setting the passband width in the Vold-Kalman order tracking filter.” In: *12th International Congress on Sound and Vibration 2005, ICSV 2005* 5 (2005), pp. 4357–4364 (cit. on pp. 31, 36).

[Van97] John Vanderkooy. “Loudspeaker ports.” In: *Audio Engineering Society Convention 103* 4523 (1997) (cit. on p. 5).

[Van98] John Vanderkooy. “Nonlinearities in Loudspeaker Ports.” In: *Audio Engineering Society Convention 104*. Vol. 4748. 1998 (cit. on p. 5).

[Whi03] F M White. *Fluid Mechanics*. {McGraw}-{Hill} international editions. McGraw-Hill, 2003. ISBN: 978-0-07-240217-9. URL: https://books.google.at/books?id=1DYtptq3OC4C (cit. on pp. 6, 11, 13, 14).

[Yve20] Yves Pene; Yoachim Horyn; and Christophe Combet. “Non-linear acoustic losses prediction in vented loudspeaker using computational fluid dynamic simulation.” In: *148th Audio Engineering Society International Convention 2020* (2020), pp. 1–10 (cit. on p. 7).

[ZF13] Eberhard Zwicker and Hugo Fastl. *Psychoacoustics: Facts and models*. Vol. 22. Springer Science & Business Media, 2013 (cit. on pp. 54–56).

[Zwi+91] Eberhard Zwicker et al. “Program for calculating loudness according to DIN 45631 (ISO 532B).” In: *Journal of the Acoustical Society of Japan (E)* 12 (1 1991), pp. 39–42. ISSN: 03882861. DOI: 10.1250/ast.12.39 (cit. on p. 51).